Transport Localization at the Percolation Transition Revealed by Betweenness Centrality: Finite-Size Scaling in Site-Diluted Archimedean Lattices

Auro Anibal Torres *, Antonio José Ramirez-Pastor, Mariela Isabel González-Flores

Posted Date: 6 April 2026

doi: 10.20944/preprints202604.0362.v1

Keywords: percolation; archimedean lattices; site dilution; transport networks; betweenness centrality; transport bottlenecks; finite-size scaling; critical phenomena,;transport susceptibility; universality

 doi:10.20944/preprints202604.0362.v1

Article

Transport Localization at the Percolation Transition Revealed by Betweenness Centrality: Finite-Size Scaling in Site-Diluted Archimedean Lattices

Auro Anibal Torres [1,*], Antonio José Ramirez-Pastor [1] and Mariela Isabel González-Flores [2]

[1] Departamento de Física, Instituto de Física Aplicada (INFAP), Universidad Nacional de San Luis–CONICET. Ejército de Los Andes 950, D5700HHW San Luis, Argentina
[2] Departamento de Física, Universidad de la Frontera, Casilla 54-D, Temuco, Chile
* Correspondence: auro.torres@gmail.com

Abstract

We investigate how transport organizes in two-dimensional Archimedean lattices under random site percolation by analyzing the scaling behavior of betweenness centrality. Transport observables are computed on the connected subgraphs formed by occupied sites as the occupation probability (p_o) is varied across the percolation transition. We show that the maximization of betweenness centrality defines a transport pseudo-critical point whose position converges to the percolation threshold (p_c) in the thermodynamic limit. Near criticality, the maximum betweenness centrality exhibits nontrivial power-law scaling with system size, consistent with the fractal geometry of the incipient infinite cluster. In particular, we find ($BC_{max} \sim L^{2d_f}$), while its variance—interpreted as a transport susceptibility—scales as ($\chi(L) \sim L^{\gamma}$), with ($\gamma \approx 4d_f$). Finite-size scaling collapses further demonstrate that both the magnitude and the fluctuations of the dominant transport bottleneck follow the universal scaling structure of two-dimensional percolation. These results are consistently observed across square, triangular, kagome, and extended kagome lattices, revealing lattice-independent critical transport behavior. Complementary measures, including the percentile (p_{90}) and inequality indicators of the betweenness distribution, show that transport criticality extends beyond extreme nodes and reflects a collective reorganization of load. Overall, our results establish a direct connection between geometric criticality and transport localization, providing a unified scaling framework for understanding critical transport phenomena in spatial networks.

Keywords: percolation; archimedean lattices; site dilution; transport networks; betweenness centrality; transport bottlenecks; finite-size scaling; critical phenomena,;transport susceptibility; universality

1. Introduction

Transport processes on complex networks are often governed by a small subset of nodes that act as bottlenecks, concentrating a disproportionate fraction of shortest paths. Betweenness centrality provides a natural quantitative measure of this phenomenon and has been widely used to characterize load distribution, vulnerability, and structural importance in networked systems [1,2]. Beyond its graph-theoretical definition, betweenness centrality captures how transport pathways reorganize under structural perturbations.

Understanding how transport bottlenecks emerge and fluctuate under structural damage is therefore central to assessing the resilience and security of networked systems [3]. Identifying the structural conditions under which transport becomes highly concentrated is of particular importance in both natural and engineered networks, where localized overload can compromise global functionality.

Percolation theory offers a classical framework to describe connectivity in disordered networks through the existence of a critical occupation probability (p_c), below which long-range connectivity is lost [4,5]. While percolation successfully characterizes the emergence of a spanning cluster, it does

 doi:10.20944/preprints202604.0362.v1

not directly address how transport routes are organized within connected components. In particular, global connectivity does not necessarily imply homogeneous transport, and strong load concentration may arise even in regimes where a macroscopic cluster is present.

This gap motivates the search for transport-based indicators that complement the geometric description provided by percolation theory. Although centrality measures have been explored in damaged or partially diluted networks [6,7], their critical scaling behavior and its relation to geometric percolation remain largely unexplored. A central question is therefore whether transport observables exhibit pseudo-critical signatures associated with the reorganization of shortest-path structures, and whether these signatures are governed by the same universal exponents that control connectivity.

In this work, we investigate betweenness centrality in two-dimensional Archimedean lattices under random site percolation. Transport observables are computed on the connected subgraphs formed by occupied sites as the occupation probability (p_o) is varied across the percolation transition. We show that the maximization of the unnormalized betweenness centrality defines a transport pseudo-critical point that converges to the percolation threshold in the thermodynamic limit.

We further demonstrate that the maximal betweenness exhibits nontrivial finite-size scaling consistent with the fractal geometry of the incipient infinite cluster. In particular, the maximum betweenness scales as a power of the system size determined by the cluster fractal dimension, while its fluctuations define a transport susceptibility that obeys universal finite-size scaling. These results are consistently observed across square, triangular, kagome, and extended kagome lattices, revealing lattice-independent critical transport behavior.

Complementary observables, including the percentile (p_{90}) and the Gini coefficient, provide additional insight into the multiscale organization of transport near critical connectivity. Together, these measures show that the emergence of transport bottlenecks is not merely an algorithmic feature of shortest-path routing, but a direct manifestation of the critical geometry of the percolation cluster.

2. Model and Methods

2.1. Network Model

2.1.1. Geometry of Archimedean Lattices

We consider two-dimensional Archimedean lattices of linear size (L) with periodic boundary conditions, ensuring translational invariance in the fully occupied limit. These lattices are regular planar graphs in which all vertices are topologically equivalent and the faces belong to a finite set of regular polygons [8,9]. In this work, we focus on four representative geometries: the square, triangular, kagome, and extended kagome (Kagome$^+$) lattices. These structures exhibit distinct local connectivities while remaining structurally comparable within the Archimedean class.

The conventional geometrical structures of the Archimedean lattices considered in this work are illustrated in Figure 1[9,10]. The lines denote lattice bonds, while their intersections correspond to lattice sites. As can be observed, the square and kagome lattices have vertices with coordination number $Z = 4$; the extended kagome lattice has coordination number $Z = 3$; whereas the triangular lattice has coordination number $Z = 6$, the largest among the Archimedean lattices.

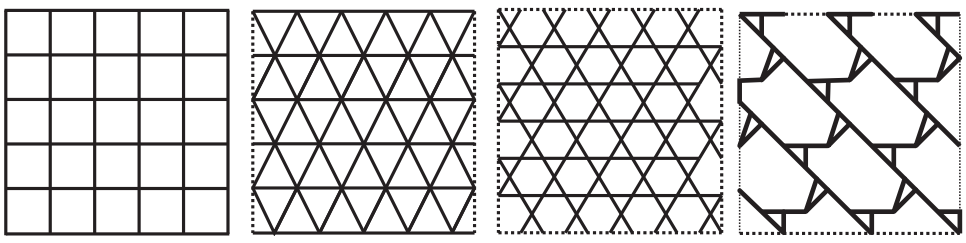

(**a**) Square (**b**) Triangular (**c**) Kagome (**d**) Kagome$^+$

Figure 1. Conventional geometric representation of the Archimedean lattices considered in this work: (a) Square: (4^4), (b) Triangular: (3^6), (c) Kagome: $(3.6.3.6)$, and (d) Extended Kagome: (3.12^2).

 doi:10.20944/preprints202604.0362.v1

Each lattice is characterized by its vertex configuration: the square lattice (4^4), the triangular lattice (3^6), the kagome lattice $(3.6.3.6)$, and the extended kagome lattice (3.12^2), indicating the sequence of polygons surrounding each vertex [8,9].

In total, there are eleven Archimedean lattices, each characterized by a distinct vertex configuration. For further details on the origin and other aspects of Archimedean lattices, we refer the reader to References[8–10].

2.1.2. Alternative Unit Cell Representation

Following Ref. [9], we employ an alternative unit cell (AUC) representation that enables a unified discrete construction across different lattices. . Figure 2 shows the conventional unit cells (CUC) in panel (a), and the alternative unit cells (AUC) in panel (b) for the four lattices considered here. The numbering of sites and bonds shown in the CUCs of Figure 2(a) corresponds to the numbering used in the AUCs of Figure 2(b).

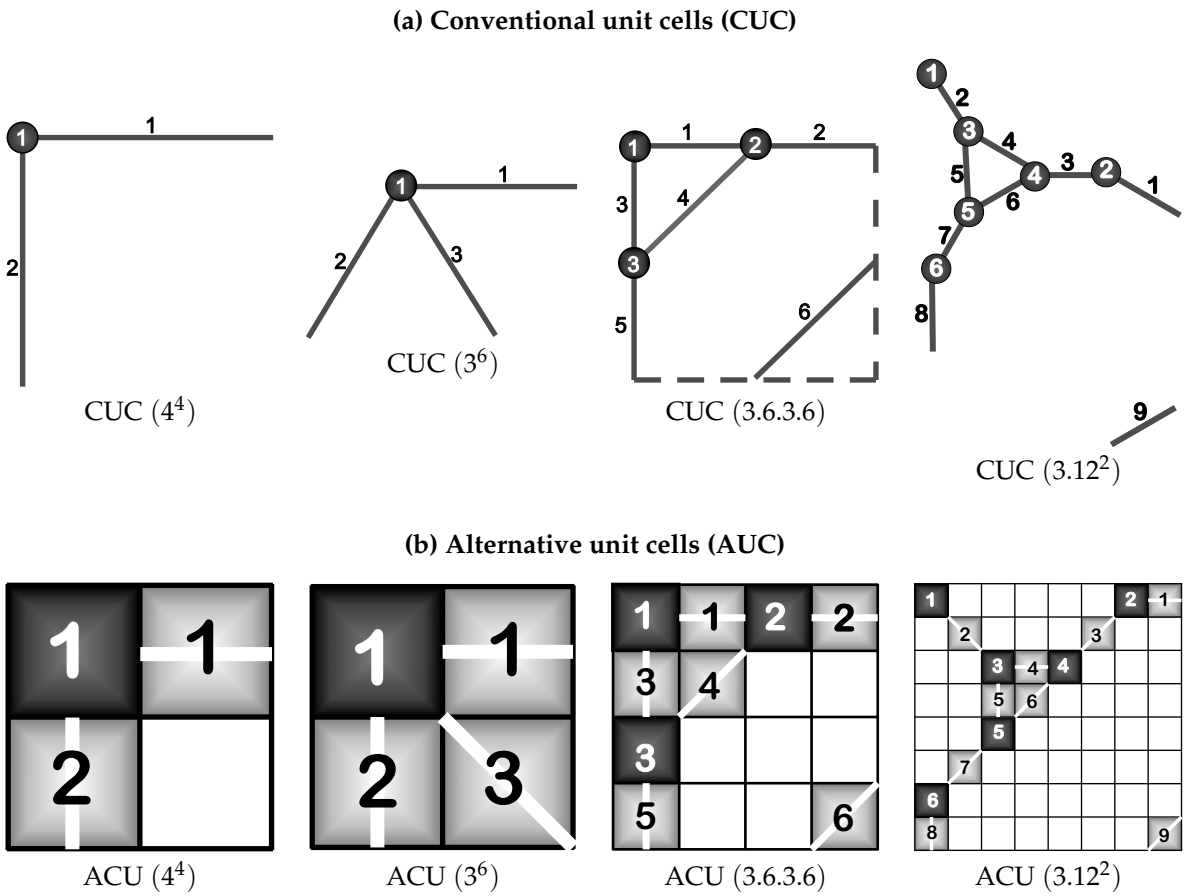

Figure 2. Conventional and alternative unit cells of the Archimedean lattices: square (4^4), triangular (3^6), kagome $(3.6.3.6)$, and extended kagome (3.12^2).

In the alternative representation, squares with a dark gray gradient denote lattice sites, squares with a lighter gray gradient denote bonds that act along the direction of the white line crossing them, while the remaining squares without shading are not used. In this representation, as in the conventional one, each site has Z bonds as first neighbors and Z sites as second neighbors. Similarly, each bond has two sites as first neighbors and $2Z - 2 = 2(Z - 1)$ bonds as second neighbors.

An additional feature of this representation is that the bonds composing the AUCs are restricted to only four orientations, namely 0° , 90° , 45° , and $135\circ$. Furthermore, the edge lengths of the polygons can be chosen as multiples of 48 within this construction [9], enabling a unified discrete representation across different lattices.

 doi:10.20944/preprints202604.0362.v1

2.1.3. Lattice Construction and Displacement Vectors

The Archimedean lattices are constructed by repeated horizontal and vertical translations of the corresponding AUC until the desired linear size L is obtained. To move across a given lattice, as many sets of displacement vectors are required as there are nonequivalent sites in its corresponding AUC. Since the present work deals exclusively with pure site percolation, it is sufficient to consider displacement vectors that connect a given site to its second-neighbor sites.

Thus, for the square and triangular lattices, whose respective AUCs contain a single site, only one set of displacement vectors is required. For the kagome lattice, three such sets are needed (three distinct site types), while for the extended kagome lattice, six sets of displacement vectors are required (six distinct site types). The total number of sites N for each lattice is determined by the AUC size and the number of distinct sites per unit cell:

$$N = \frac{(\text{number of sites per AUC}) \times L^2}{(\text{AUC area})}. \tag{1}$$

Specifically:

- Square lattice: 1 site per AUC, AUC area $= 4 \rightarrow N = L^2/4$
- Triangular lattice: 1 site per AUC, AUC area $= 4 \rightarrow N = L^2/4$
- Kagome lattice: 3 sites per AUC, AUC area $= 16 \rightarrow N = 3L^2/16$
- Extended Kagome lattice: 6 sites per AUC, AUC area $= 64 \rightarrow N = 6L^2/64$

Table 1 lists the sets of displacement vectors used to connect each site in the AUC to its second-neighbor sites. The notation employed in the tables is sif and sic, where i labels the site within the AUC, and the vectors correspond to displacements along the vertical (f) and horizontal (c) directions of the AUC representation, respectively, following the standard matrix convention where f denotes rows and c denotes columns.

 doi:10.20944/preprints202604.0362.v1

Table 1. Sets of displacement vectors connecting the sites contained in the AUC to its second-neighbor sites (2NN). The notation employed in the tables is sif and sic, where i labels the site within the AUC, and the vectors correspond to displacements along the vertical (f) and horizontal (c) directions of the AUC representation, respectively, following the standard matrix convention where f denotes rows and c denotes columns. (a) For the square lattice (left) and the triangular lattice (right). Both with a site in its AUC, respectively. (b) For the kagome lattice (left), which contains three sites in its AUC, and for the extended kagome lattice (right), whose AUC contains six sites.

a Square lattice (left) and the triangular lattices (right).

(4^4)					(3^6)						
Displacements	2NN				Displacements	2NN					
$s1f=$	-2	0	+2	0	$s1f=$	-2	0	+2	0	-2	+2
$s1c=$	0	-2	0	+2	$s1c=$	0	-2	0	+2	-2	+2

b Kagome lattice (left), and the extended kagome lattices (right).

(3.6.3.6)								(3.12^2)			
Displacements				**2NN**				**Displacements**	**2NN**		
$s1f=$				-2	0	+2	0	$s1f=$	-2	0	+2
$s1c=$				0	-2	0	+2	$s1c=$	0	-2	+2
$s2f=$				0	+2	0	-2	$s2f=$	+2	0	-2
$s2c=$				-2	-2	+2	+2	$s2c=$	-2	+2	+2
$s3f=$				-2	+2	+2	-2	$s3f=$	-2	+2	0
$s3c=$				0	-2	0	+2	$s3c=$	-2	0	+2
-	-	-	-	-	-	-	-	$s4f=$	0	+2	-2
-	-	-	-	-	-	-	-	$s4c=$	-2	-2	+2
-	-	-	-	-	-	-	-	$s5f=$	-2	+2	-2
-	-	-	-	-	-	-	-	$s5c=$	0	-2	+2
-	-	-	-	-	-	-	-	$s6f=$	+2	+2	-2
-	-	-	-	-	-	-	-	$s6c=$	-2	0	+2

For the square lattice, whose AUC contains a single site, only one set appears:

$$s1f = (-2, 0, +2, 0)\ ,\ s1c = (0, -2, 0, +2)$$

These define the displacement vectors $(-2,0), (0,-2), (2,0), (0,2)$, connecting the unique site to its second-neighbor sites. The triangular lattice follows an analogous scheme with six displacement vectors. For the kagome lattice, three sets are required ($i = 1, 2, 3$), and for the extended kagome lattice, six sets ($i = 1, 2, 3, 4, 5, 6$).

Although these displacements connect second-neighbor sites in the AUC representation, they define the nearest-neighbor connectivity of the effective lattice implemented in the C++ code for the transport calculations (betweenness centrality, cluster analysis, etc.).

2.1.4. Site-type Identification and Neighbor Selection

In lattices whose AUC contains multiple nonequivalent sites, it is necessary to determine, for a given lattice position (f, c), which site type is being visited in order to apply the appropriate set of displacement vectors. This identification is performed through a modular mapping with respect to the dimensions of the AUC.

Let F and C denote the number of rows and columns of the AUC, respectively. Any lattice coordinate (f, c) can be mapped onto a position within the AUC through the pair (f mod F, c mod C). This reduced coordinate uniquely identifies the type of site associated with (f, c), and therefore determines which set of displacement vectors (sif, sic) must be used to define its connectivity.

 doi:10.20944/preprints202604.0362.v1

As an illustrative example, consider the kagome lattice, whose AUC contains three distinct site types. In this case, the mapping is given by

$$(f \bmod F, c \bmod C) = \begin{cases} (0,0) & \rightarrow \text{type} \quad 1, \\ (0,2) & \rightarrow \text{type} \quad 2, \\ (2,0) & \rightarrow \textit{type} \quad 3. \end{cases}$$

Once a site is identified as belonging to a given type i, the corresponding displacement vector are used to generate the positions of its neighboring sites. For lattices with a single site per AUC, such as the square and triangular lattices, the mapping becomes trivial and the connectivity can be directly obtained from the regular grid indexing.

The neighbor-selection procedure can be summarized as follows:

1. For each site (f, c), compute $(f_0, c_0) = (f \bmod F, c \bmod C)$
2. Identify site type i from the modular mapping
3. For each displacement vector k:
   (a) Compute $(n_f, n_c) = (f + sif[k], c + sic[k])$
   (b) Apply periodic boundary conditions
   (c) Add the neighbor if the corresponding site exists

This procedure directly defines the adjacency structure of the lattice, which constitutes the input for the transport calculations. The resulting network is represented as a graph where nodes correspond to lattice sites and edges are established between pairs of sites identified as neighbors through the displacement-vector scheme.

2.1.5. Network Filling

Once the lattice connectivity has been established, disorder is introduced by randomly vacating sites. Starting from a fully occupied lattice, each site is independently vacated with probability p_v. The remaining occupied sites and their associated edges define the diluted network.

Transport observables are computed on the connected subgraphs formed by the occupied sites, which constitute a fraction $p_o = 1 - p_v$ of the total sites. For each pair (L, p_o), statistical averages are obtained over a large number of independent realizations, as described in the following sections.

2.2. Monte Carlo Simulation Protocol

We employ a site percolation model where each site is initially occupied. For a given vacancy probability p_v, a fraction p_v of sites is randomly vacated, leaving an occupation probability $p_o = 1 - p_v$. The simulation follows an adaptive sampling strategy to achieve high statistical accuracy near the percolation threshold $p_v^c(L)$. The expected percolation threshold for each lattice is estimated using finite-size scaling relations:

$$\begin{aligned} p_v^{c,\text{square}}(L) &= 1 - \left(0.59307 - 0.43L^{-0.75}\right) \\ p_v^{c,\text{triangular}}(L) &= 1 - \left(0.4998 - 0.373L^{-0.75}\right) \\ p_v^{c,\text{Kagome}}(L) &= 1 - \left(0.65319 - 0.458L^{-0.75}\right) \\ p_v^{c,\text{Ext.Kagome}}(L) &= 1 - \left(0.59307 - 0.43L^{-0.75}\right) \end{aligned}$$

Note that $p_v^c(L) = 1 - (p_c - aL^{-0.75})$ here represents the critical vacancy probability. The different scaling relations of the form $p_c - aL^{-0.75}$ were obtained from Torres et al.[9].

The set of $p_v$values is generated adaptively:

- Far from p_v^c ($|p_v - p_v^c| > 0.15$): step size $\Delta p_v = 0.05$
- Intermediate region ($0.05 < |p_v - p_v^c| \leq 0.15$): step size $\Delta p_v = 0.05$ with increased sampling

 doi:10.20944/preprints202604.0362.v1

- Near p_v^c ($|p_v - p_v^c| \leq 0.05$): step size $\Delta p_v = 0.01$ with maximum sampling

The number of independent configurations M for each p_v is:

$$M(p_v) = \begin{cases} M_0 & \text{if} \quad |p_v - p_v^c| > 0.1 \\ 5M_0 & \text{if} \quad 0.05 < |p_v - p_v^c| \leq 0.1 \\ 10M_0 & \text{if} \quad |p_v - p_v^c| \leq 0.05 \end{cases}$$

with baseline $M_0 = 1000$ configurations. This adaptive scheme ensures statistical convergence while maintaining computational efficiency. For each configuration, the network is constructed by retaining only occupied sites (those not vacated) and the edges connecting them according to the adjacency rules defined in Section 2.1.

2.3. Betweenness Centrality and Transport Observables

2.3.1. Betweenness Centrality

Transport on the diluted lattices is characterized through betweenness centrality of the occupied nodes graph $\mathcal{G}(p_o)$. For a given node $u \in \mathcal{G}$, the intrinsic o unnormalized betweenness centrality $BC(u)$ is defined as

$$BC(u; p_o) = \sum_{\substack{s \neq u \neq t \\ s,t \in G(p_o)}} \frac{\sigma_{st}(u)}{\sigma_{st}}, \tag{2}$$

where σ_{st} is the total number of shortest paths between nodes s and t, and $\sigma_{st}(u)$is the number of those paths that pass through node u. The sum runs over all ordered pairs of distinct nodes belonging to the same connected component of the diluted network.

This definition assigns to each node a quantitative measure of its participation in shortest-path transport across the network. In particular, nodes with high betweenness centrality act as transport bottlenecks, concentrating a significant fraction of geodesic paths.

To obtain a normalized measure that allows for meaningful comparisons across different system sizes and occupation densities, we consider

$$BC^N(u; p_o) = \frac{BC(u; p_o)}{(N-1)(N-2)/2} \tag{3}$$

where N is the total number of nodes in the lattice (occupied and vacant). This normalization differs from the standard one in network theory, which typically uses the number of nodes in the graph, in this case the number of occupied sites $N_o = p_o N$.

Our choice is motivated by the fact that, in percolation problems, the total lattice size N remains fixed as the occupied o vacancy concentration varies. Normalizing by N therefore provides a common baseline independent of p_o, allowing us to compare centrality values across different occupation probabilities without the distortion introduced by the changing size of the occupied cluster. Furthermore, this normalization preserves the natural scaling with system size in the thermodynamic limit and is consistent with standard finite-size scaling analyses in statistical physics.

We compute $BC(u, p_o)$ for all occupied sites using Brandes' algorithm [11], which has time complexity $O(N_o(N_o + E_o))$ for unweighted graphs, where E_o is the number of edges in $\mathcal{G}(p_o)$. The network is treated as undirected. Thus, two occupied nodes are considered connected if there exists a path between them consisting entirely of occupied nodes, regardless of direction.

2.3.2. Transport Observables

From the distribution of betweenness values among occupied sites, we extract three key metrics:

 doi:10.20944/preprints202604.0362.v1

1. **Maximal betweenness centrality**

$$BC_{max}(p_o, L) = \max_{u \in \mathcal{G}(p_o)} BC(u; p_o), \tag{4}$$

which quantifies the load concentrated on the most critical bottleneck of the network.

2. **High-order percentiles**
We consider high-order percentiles of the betweenness distribution. In particular the 90th percentile p_{90} is defined as the value of betweenness below which 90% of the nodes fall. This observable captures the behavior of highly loaded nodes beyond the single dominant bottleneck and provides information on the upper tail of the transport distribution. The normalization of p_{90} is similar to that of BC.

3. **Inequality measures**
To quantify global heterogeneity in transport organization, we compute the Gini coefficient G, defined as

$$G = \frac{2\sum_{i=1}^{n} x_{(i)}}{N_o \sum_{i=1}^{n} x_i} - \frac{N_o + 1}{N_o} \tag{5}$$

where $x_{(1)} \leq x_{(2)} \leq \cdots \leq x_{(n)}$ are the sorted betweenness values of the N_o occupied sites. The Gini coefficient provides a global measure of load heterogeneity, ranging from zero for perfectly homogeneous transport to one in the limiting case where all betweenness is concentrated on a single node.

These observables provide complementary information on transport organization, ranging from extreme bottlenecks to multiscale load heterogeneity patterns.

To illustrate the behavior of the transport observables defined above, Figure 3 presents representative configurations of a site-diluted triangular lattice of size 6AUC $\times$ 6AUC $= 6 \times$ 6AUC for different occupation probabilities p_o. The panels show the spatial distribution of betweenness centrality, highlighting both the maximum value BC_{max} and the heterogeneity of the distribution as quantified by the Gini coefficient G.

Active (occupied) sites are represented by green disks whose radii are proportional to their BC values. The site with maximum BC is highlighted by a concentric red disk with half the radius. Active links are shown as yellow disks of the same radius.

 doi:10.20944/preprints202604.0362.v1

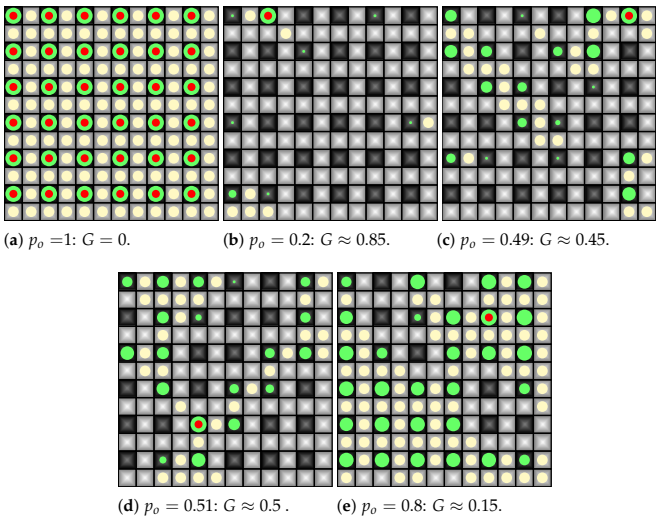

(**a**) p_o =1: $G = 0$. (**b**) $p_o = 0.2$: $G \approx 0.85$. (**c**) $p_o = 0.49$: $G \approx 0.45$.

(**d**) $p_o = 0.51$: $G \approx 0.5$. (**e**) $p_o = 0.8$: $G \approx 0.15$.

Figure 3. Visualization of transport heterogeneity through betweenness centrality (BC) in a site-diluted triangular lattice for different occupation probabilities p_o . All panels correspond to systems of size 6×6 AUC. Active sites are represented by green disks whose radii are proportional to their BC values. The site with maximum BC is highlighted by a concentric red disk with half the radius. Active links are shown as yellow disks of the same radius. The Gini coefficient G is reported as an approximate measure of inequality in the BC distribution. (a) p_o =1: fully occupied lattice. All sites have identical BC ($BC = 24$), resulting in a homogeneous transport pattern with $G = 0$. (b) $p_o = 0.2$: strongly subcritical regime. The network is highly fragmented, with a single dominant BC maximum. No spanning cluster is present, and transport is highly localized, yielding a large inequality ($G \approx 0.85$). (c) $p_o = 0.49$: near-critical regime below the percolation threshold. Although several sites exhibit comparable BC values, a single maximum still dominates. The largest cluster does not percolate, and the system displays intermediate heterogeneity ($G \approx 0.45$). (d) $p_o = 0.51$: near-critical regime above the percolation threshold. A spanning cluster emerges, and the maximum-BC site belongs to it. Multiple high-BC nodes are observed, reflecting the formation of competing transport channels ($G \approx 0.5$). (e) $p_o = 0.8$: supercritical regime. The giant component dominates the network, and although several sites have comparable BC values, transport becomes more evenly distributed, leading to a lower inequality ($G \approx 0.15$). These panels illustrate the emergence of transport heterogeneity near the percolation threshold and its subsequent homogenization deep in the supercritical regime.

(a) In the fully occupied case, transport is homogeneous and all sites share the same centrality. (b) In contrast, deep in the subcritical regime, transport is highly localized and dominated by a small number of nodes, leading to large values of G. (c) and (d) Near the percolation threshold, the system exhibits strong fluctuations, with the emergence of bottlenecks characterized by large BC values. (e) Above the threshold, the formation of a spanning cluster redistributes transport across multiple competing paths, reducing the overall inequality.

These configurations provide a qualitative interpretation of the observables BC_{max} and G, and anticipate their critical behavior analyzed in the following sections.

2.4. Cluster Analysis

The percolation properties are characterized by the size of the largest connected cluster S_{max}. After vacating sites with probability p_v, we identify clusters using breadth-first search (BFS) over occupied sites. The cluster size is defined as the number of occupied sites in the largest connected component. This quantity serves as the order parameter for the percolation transition, with $Smax \approx 0$ below the percolation threshold and $Smax \sim O(N_o)$ above it.

The algorithm proceeds as follows:

1. Initialize a visited array of size N to false
2. For each occupied site not yet visited:
   (a) Perform BFS to identify all connected occupied sites

 doi:10.20944/preprints202604.0362.v1

(b) Record the cluster size
(c) Update S_{max} if the current cluster exceeds the previous maximum

3. Return S_{max} as the size of the largest cluster

2.5. Statistical Analysis

For each value of p_v, we compute the sample mean $\bar{X}$ and standard deviation STD_X over $M(p_v)$ independent configurations:

$$\bar{X} = \frac{1}{M}\sum_{i=1}^{M} X_i,\ STD_X = \sqrt{\frac{1}{M}\sum_{i=1}^{M}(X_i - \bar{X})^2} \tag{6}$$

where X represents any of the measured quantities (BC_{max}, G, p_{90}, or S_{max}). The reported results include both the mean and the standard deviation to characterize the statistical fluctuations. The standard deviations (STD) are normalized in a manner similar to that of BC y p_{90}.

2.6. Critical-Point Simulations

For the determination of critical-point observables, the same simulation protocol described in Sections 2.2-2.5 was employed but restricted to the critical vacancy probability $p_v^c = 1 - p_c$, where p_c is the critical occupation threshold in the thermodynamic limit. For these runs, the number of independent configurations was fixed at $M = 100M_0 = 100000$ to minimize statistical fluctuations near the transition. The measured quantities at p_v^c include BC_{max}, G, p_{90}, S_{max}, and their respective standard deviations .

2.7. Determination of the Optimal Vacancy Probability

To locate the value of p_v that maximizes the maximum betweenness centrality BC_{max}, we employed a two-stage optimization procedure based on the golden section search method [12].

Initial exploration. For each lattice type and size L, we first evaluated BC_{max} at a small set of initial p_v values. The set was chosen based on preliminary estimates of the peak location for each system size. The point yielding the highest BC_{max} was selected as the initial guess p_{init}.

Golden section search. The candidate maximum was then refined using the golden section search algorithm. Given an initial interval $[a, b] = [p_{\text{init}} - \delta, p_{\text{init}} + \delta]$, where δ is an adaptive parameter depending on L (Table), the algorithm evaluates the objective function $f(p_v) = BC_{max}(p_v)$ at two interior points defined by the golden ratio conjugate $\phi = \left(\sqrt{5} - 1\right)/2 \approx 0.618$:

$$x_1 = b - \phi(b - a),\ x_2 = a + \phi(b - a).$$

The interval is updated by comparing $f(x_1)$ and $f(x_2)$:

- if $f(x_1) < f(x_2)$, the candidate maximum lies in $[x_1, b]$
- Otherwise, the candidate maximum lies in $[a, x_2]$

The procedure continues until the interval width falls below a tolerance $\epsilon = 10^{-5}$. The optimal point is taken as the midpoint of the final interval, $p_v^* = (a + b)/2$.

For each evaluation of $f(p_v)$, a single configuration was generated by randomly vacating sites with probability p_v and computing BC_{max} using the Brandes algorithm [11]. To obtain statistically robust estimates, the entire optimization procedure was repeated over $N_{\text{curves}} = 10000$ independent realizations, each with a different random seed. The reported p_v^* is the average over these realizations, and its uncertainty is given by the standard deviation.

Post-processing. After determining p_v^*, the corresponding maximum betweenness $BC_{max}(p_v^*)$ was normalized by the factor $K = 2/[(N-1)(N-2)]$ to obtain BC_{max}^N. Additionally, the Gini coefficient,

 doi:10.20944/preprints202604.0362.v1

Table 2. Adaptive interval half-width δ used in the golden section search as a function of system size L.

L	δ
≤ 24	0.014
≤ 48	0.0085
≤ 96	0.004
≤ 144	0.002
≤ 192	0.001
≥ 240	0.0007

90th percentile, and largest cluster size at p_v^* were recorded to characterize the system at the optimal point.

2.8. Overview of Simulation Programs

The three computational programs developed in this work share the same algorithmic core but differ in their objectives. The main characteristics of each program are summarized in the following list:

Program 1 – Full Curves

- **Objective:** Generate complete curves of $BC_{max}(p_v)$, G, $p_{90}(p_v)$, and $S_{max}(p_v)$
- p_v **range:** Adaptive from 0 to 1, with step size 0.05 far from $p_v^c(L)$ and 0.01 near $p_v^c(L)$
- **Sampling strategy:** Adaptive, with $M_0 = 1000$ configurations far from $p_v^c(L)$ and up to $10M_0$ near $p_v^c(L)$
- **Output:** Full curves for all metrics

Program 2 – Critical-Point Values

- **Objective:** Compute BC_{max}, G, p_{90}, and S_{max} at the percolation threshold $p_v = 1 - p_c$
- p_v **range:** Single value $p_v = 1 - p_c$
- **Sampling strategy:** Fixed at $M = 100M_0 = 100000$ configurations
- **Output:** Critical-point estimates for each lattice type and size

Program 3 – Maximum of BC_{max}

- **Objective:** Determine the vacancy probability p_v^* that maximizes BC_{max}^N, using golden section search
- p_v **range:** Dense around the peak, refined by golden section search
- **Sampling strategy:** Single configuration per function evaluation; $N_{\text{curves}} = 10000$ independent realizations
- **Output:** p_v^*, BC_{max}^N, G, p_{90}, and S_{max} at the optimal point p_v^*

2.9. Summary of Notation

For convenience, the following list summarizes the notation used throughout this work.

- L: Linear size of the lattice
- N: Total number of sites in the fully occupied lattice
- Z: Coordination number (number of neighbors per site)
- p_v: Vacancy probability (fraction of sites removed)
- $p_o = 1 - p_v$: Occupation probability
- p_v^c: Critical vacancy probability (percolation threshold)
- p_v^*: Vacancy probability that maximizes BC_{max}
- $M(p_v)$: Number of independent configurations for a given p_v
- $M_0 = 1000$: Baseline number of configurations
- $N_{\text{curves}} = 10000$: Number of independent realizations for optimization

 doi:10.20944/preprints202604.0362.v1

- $BC(u)$: Betweenness centrality of node u
- BC_{max}: Maximum betweenness among occupied sites
- BC^N_{max}: Normalized maximum betweenness (KBC_{max})
- G: Gini coefficient of betweenness distribution
- p_{90}: 90th percentile of betweenness distribution
- S_{max}: Size of the largest connected cluster
- K: Normalization factor for BC_{max} y p_{90}
- δ: Adaptive interval half-width for golden section search
- $\epsilon = 10^{-5}$: Convergence tolerance for golden section search

3. Results

3.1. Betweenness Maximization, 90th Percentile, and Susceptibility Under Site Dilution

3.1.1. Betweenness Maximization and Transport Pseudo-critical Point

We begin by analyzing the behavior of the maximum betweenness centrality, as a function of the occupation probability p_o for the four Archimedean lattices considered in this work: square, triangular, kagome, and extended kagome (Kagome$^+$). For each system size L, the lattice is initially fully occupied and sites are randomly removed until the desired occupation fraction p_o is reached. Betweenness centrality is computed on the remaining connected subgraph, and the maximum value over all occupied sites is recorded.

To illustrate the intrinsic scaling of the observable and the effect of normalization, Figure 4 shows the unnormalized quantity $BC_{max}(L, p_o)$ (in logarithmic scale), as a function of p_o, while Figure 5 displays its normalized counterpart $BC^N_{max}(L, p_o)$, for all lattices and system sizes $L = 48, 96, 192, 384$. As shown in Figure 4, the maximum of $BC_{max}(L, p_o)$ increases systematically with system size across all lattices, reflecting the growing number of shortest paths that concentrate on the dominant transport nodes as the network becomes larger. This behavior is expected, as larger systems offer more potential paths, allowing the betweenness of central nodes to grow.

In contrast, Figure 5 shows the normalized maximum betweenness $BC^N_{max}(L, p_o)$, where the normalization factor $K = 2/[(N-1)(N-2)]$ removes the trivial scaling with the total number of node pairs. Here, the peak height decreases with increasing L. This apparent reduction does not reflect a weakening of transport concentration, but rather arises from the normalization factor, which grows slower than BC_{max} with system size, effectively compensating for the increase observed in Figure 4.

In all cases, $BC^N_{max}(L, p_o)$ exhibits a clear non-monotonic behavior. Starting from high occupation fractions ($po \approx 1$), BC^N_{max} increases as dilution induces the formation of preferential transport paths. Beyond a certain dilution level, however, the progressive fragmentation of the network suppresses long-range connectivity, leading to a decrease of BC^N_{max}. As a result, a well-defined maximum emerges at an intermediate value $p^c_o(L)$.

This maximum defines a **transport pseudo-critical point**, distinct from but closely related to the standard percolation threshold.

We define $p^c_o(L)$ as the occupation fraction at which the maximal betweenness attains its maximum value:

$$p^c_o(L) = \arg\max_{p_o} BC_{max}(L, p_o) \tag{7}$$

which is equivalent to the location of the maximum of $BC^N_{max}(L, p_o)$, since normalization does not affect its position. This definition is purely transport-based and does not rely on connectivity criteria, but instead identifies the point of maximal flow concentration within the network. Following the notation used in Section 2.7, this corresponds to $p^c_o(L) = 1 - p^*_v(L)$ where $p^*_v(L)$ is the vacancy probability that maximizes BC^N_{max}.

For each system size, $p^c_o(L)$ is determined numerically from the location of the peak. Owing to the sizable sample-to-sample fluctuations of the observable, the peak position is identified within a

 doi:10.20944/preprints202604.0362.v1

finite uncertainty interval. Nevertheless, the resulting estimates are sufficiently stable to reveal a clear and systematic finite-size trends.

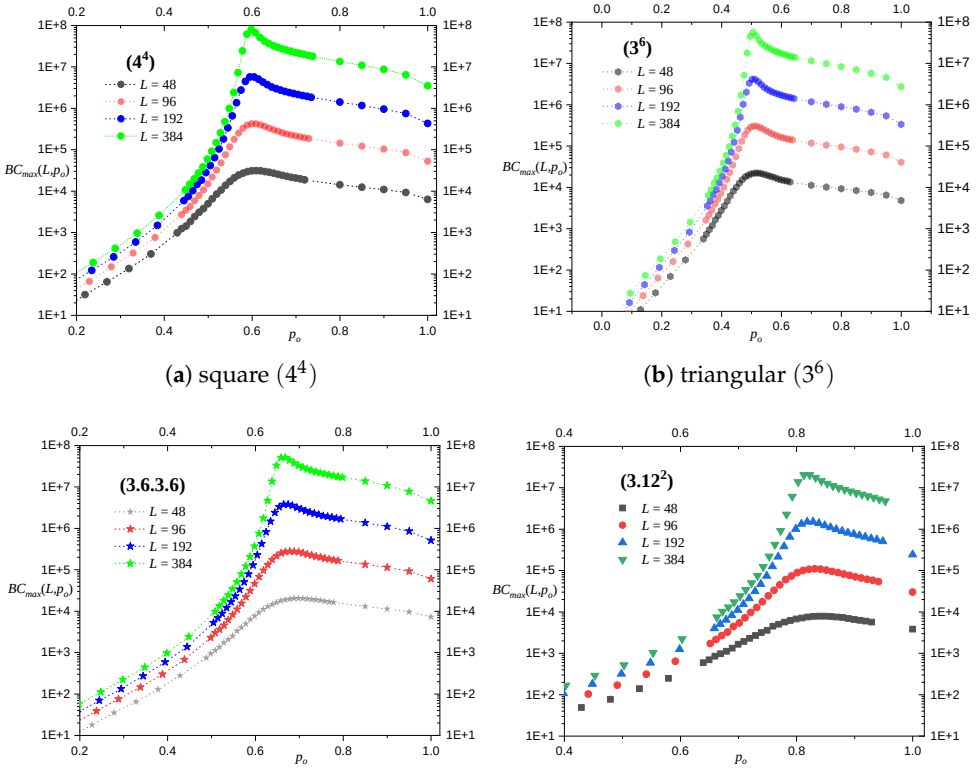

(**a**) square (4^4) (**b**) triangular (3^6)

(**c**) kagome $(3.6.3.6)$ (**d**) Extended kagome (3.12^2)

Figure 4. Maximum betweenness centrality, $BC_{max}(L, p_o)$ (in logarithmic scale) , as a function of the occupation concentration p_o for system sizes $L = 48, 96, 192, 384$. **(a)** square (4^4), **(b)** triangular (3^6), **(c)** kagome $(3.6.3.6)$, and **(d)** extended kagome lattices (3.12^2). The maximum of $BC_{max}(L, p_o)$ increases systematically with system size across all lattices, reflecting the growing number of shortest paths that concentrate on the dominant transport nodes as the network becomes larger.

 doi:10.20944/preprints202604.0362.v1

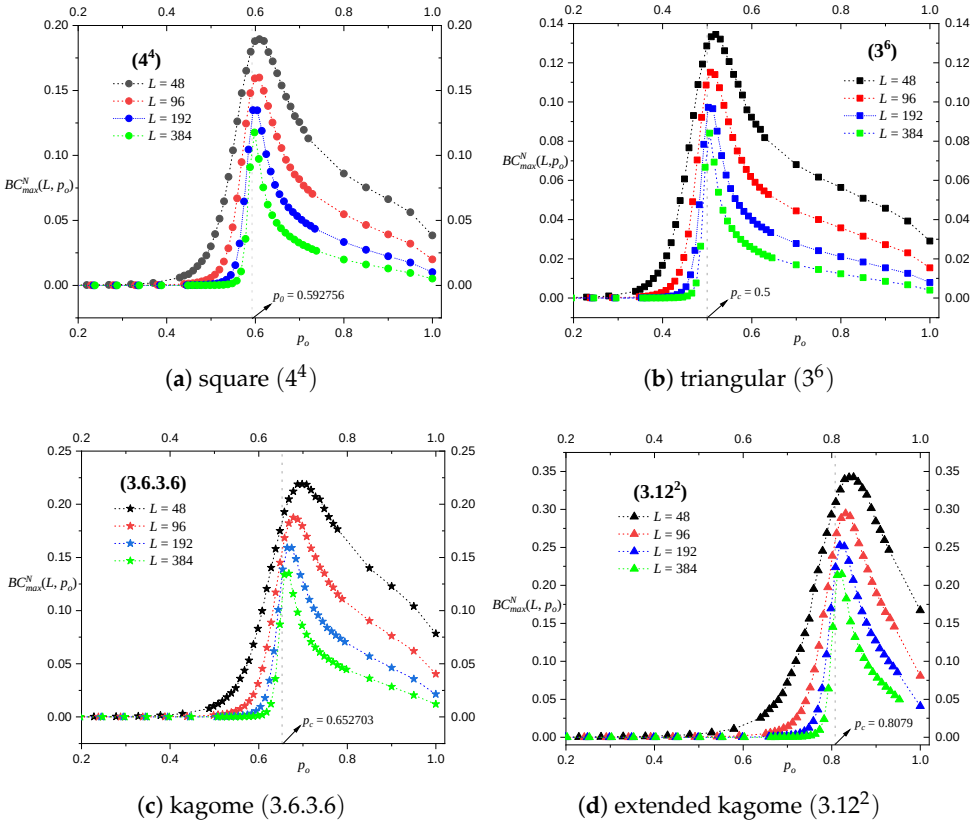

(**a**) square (4^4) (**b**) triangular (3^6)

(**c**) kagome $(3.6.3.6)$ (**d**) extended kagome (3.12^2)

Figure 5. Maximum betweenness centrality, $BC^N_{max}(L, p_o)$, as a function of the occupation concentration p_o for different system sizes L in the **(a)** square (4^4), **(b)** triangular (3^6), **(c)** kagome $(3.6.3.6)$, and **(d)** extended kagome lattices (3.12^2). All lattices exhibit a clear non-monotonic dependence with a well-defined maximum at an intermediate occupation concentration $p_o^c(L)$, signaling the existence of a transport pseudo-critical point. As the system size increases, the peak becomes progressively sharper while its amplitude decreases. Vertical dotted lines indicate the value p_c , where p_c is the percolation threshold of occupied sites of each lattice in the thermodynamic limit. For all system sizes, the maxima occur at occupation concentrations above this value and shift progressively toward it as the system size increases.

3.1.2. 90th Percentile

To further characterize the role of highly central nodes beyond the absolute maximum, we consider the percentile p_{90} of the betweenness centrality distribution, defined as the value below which 90% of the nodes fall. This quantity provides information about the upper tail of the distribution while reducing the influence of extreme fluctuations associated with a single node. For clarity, and given that the qualitative behavior of this observable is found to be robust across all considered lattices, we restrict the detailed analysis of p_{90} to the square lattice as a representative case.

Figure 6(a) shows $p_{90}(p_o)$ for different system sizes. Qualitatively, the curves exhibit a peak-like structure similar to that observed for BC^N_{max}, with a maximum located in the vicinity of the percolation threshold and a progressive sharpening as the system size increases. This behavior indicates that not only the most central node, but a finite fraction of highly central nodes, becomes increasingly relevant near criticality.

Preprints.org (www.preprints.org) | NOT PEER-REVIEWED | Posted: 6 April 2026 doi:10.20944/preprints202604.0362.v1

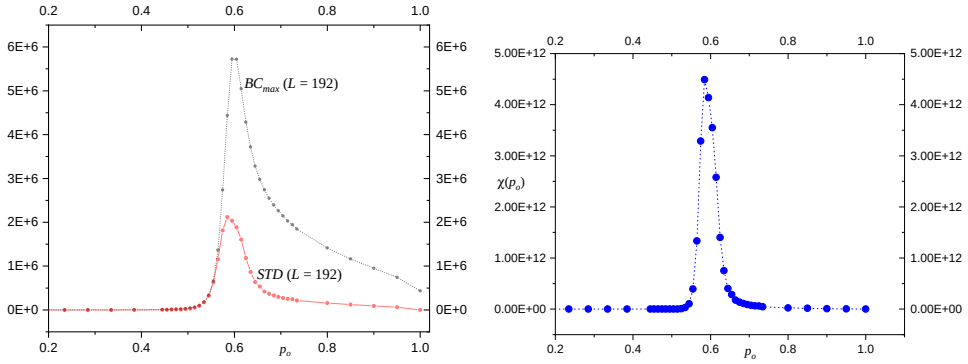

(**a**) STD and BC_{max} vs p_o. (**b**) χ vs p_o.

Figure 7. Fluctuations and susceptibility associated with the maximum betweenness centrality as a function of the occupation probability p_o for the square lattice (4^4) at system size $L = 192$. (a) STD and BC_{max} vs p_o, (b) χ vs p_o.

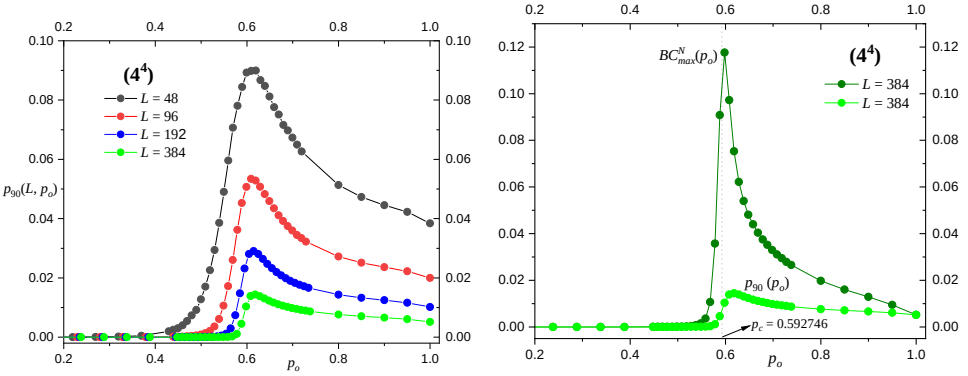

(**a**) p_{90} vs p_o for the square lattice. (**b**) p_{90} and BC^N_{max} vs p_o for $L = 384$ (square lattice).

Figure 6. Behavior of the percentile p_{90} of the betweenness centrality distribution under site dilution. Panel (a) shows p_{90} as a function of the occupation probability p_o for different system sizes of the square lattice. The curves exhibit a peak-like structure in the vicinity of the percolation threshold that becomes sharper as the system size increases. Panel (b) compares p_{90} with the normalized maximum betweenness centrality BC^N_{max} for a fixed system size of the square lattice. While both observables display a maximum near the percolation threshold, the peak of p_{90} is significantly lower and broader, indicating a smoother and less localized response.

However, important differences arise when comparing both observables directly. As shown in Figure 6(b) for $L = 384$, the peak of p_{90} is significantly lower and broader than that of BC^N_{max}, and its maximum is slightly shifted away from the critical point. These features reflect the fact that p_{90} captures a collective property of the upper tail of the distribution, rather than the behavior of a single extremal node.

Taken together, these results indicate that while BC^N_{max} provides a sharp and well-localized signature of the percolation transition, the percentile p_{90} yields a smoother and less localized response, probing a wider set of nodes that participate in the transport backbone. A comparison with global measures of transport heterogeneity will be discussed in the following subsection 3.2.

3.1.3. Transport Susceptibility

In addition to the average behavior, the fluctuations of the maximum betweenness centrality provide further insight into the transport properties of the system. Figure 7 shows the standard deviation STD of BC_{max} as a function of the occupied concentration p_o for the square lattice at $L = 192$.

The standard deviation exhibits a pronounced peak in the vicinity of the pseudo-critical point, indicating enhanced sensitivity of transport pathways to microscopic disorder in this regime. This behavior reflects the strong realization-to-realization variability of load concentration when the system

 doi:10.20944/preprints202604.0362.v1

is near the transition between globally connected and fragmented transport structures. Away from this region, the fluctuations decrease rapidly as transport becomes either more homogeneous at low vacancy concentrations (high occupancy) or strongly suppressed at high dilution (low occupancy). The same qualitative behavior is observed for all system sizes and across the different Archimedean lattices considered, confirming that enhanced transport fluctuations are an intrinsic feature of the pseudo-critical regime.

The peak in the fluctuations of BC_{max} near $p_o^c(L)$ can be naturally interpreted as a manifestation of an effective transport susceptibility. In analogy with critical phenomena, where response functions quantify the sensitivity of the system to small perturbations, the standard deviation of BC_{max} measures the susceptibility of transport pathways to microscopic structural disorder. Near the pseudo-critical point, small changes in site occupancy can induce large reorganizations of shortest-path structures, resulting in significant variability in both the magnitude and spatial localization of the dominant transport pathways. This behavior reflects the marginal stability of the transport backbone in this regime, where the network is poised between global connectivity and fragmentation. Away from the pseudo-critical region, transport structures become either robust or strongly suppressed, and the susceptibility correspondingly decreases. This susceptibility peak therefore signals the regime of maximal structural vulnerability and transport localization, analogous to the fluctuation peak observed at the percolation transition.

Motivated by this interpretation, we formally define an effective transport susceptibility as

$$\chi(L, p_o) = \mathrm{var}(BCmax(L, p_o)) = \left\langle BC_{max}^2 \right\rangle - \langle BC_{max} \rangle^2 \tag{8}$$

where $\mathrm{var} = STD^2$ is the variance and the averages are taken over independent realizations of the disorder. This quantity measures realization-to-realization fluctuations in transport load concentration. As shown in panel (a) of the Figure 7, the standard deviation of BC_{max} exhibits a pronounced maximum near the pseudo-critical point. By definition, the susceptibility $\chi_{BC_{max}}$ also exhibits a maximum in this region, as shown in panel (b), confirming the critical nature of the transport pseudo-transition.

A quantitative analysis of the finite-size scaling of this transport susceptibility will be presented in Section 3.6.

3.2. Transport Heterogeneity: Gini Coefficient

The behavior of the transport observables under site dilution is first characterized through the maximum betweenness centrality BC_{max}^N, the percentile p_{90} and the Gini coefficient G, all evaluated as functions of the occupation probability p_o for different system sizes.

The quantity $BC_{max}^N(p_o)$ exhibits a well-defined peak located near the percolation threshold. Its shape resembles a concave-down curve centered around the critical point, and becomes progressively sharper as the system size increases, reflecting the growing localization of transport at criticality. In this case, the position of the maximum and the center of the peak are essentially aligned, indicating that BC_{max}^N provides a direct signature of the structural transition in the network.

A similar, though less pronounced, behavior is observed for the percentile $p_{90}(p_o)$, which probes the upper tail of the betweenness centrality distribution. As shown in Figure 6, $p90$ also displays a peak-like structure in the vicinity of the percolation threshold, with a maximum that remains close to p_c but is slightly shifted and significantly broader than that of BC_{max}^N. In addition, the height of the peak is substantially reduced, indicating that the collective contribution of highly central nodes leads to a smoother and less localized response.

To quantify the global heterogeneity of transport, we analyze the Gini coefficient $G(p_o)$. As shown in Figure 8, G increases as the system is diluted, starting from $G = 0$ in the fully occupied lattice and reaching large values in the subcritical regime, where transport becomes highly localized. Similarly to BC_{max}^N, the Gini coefficient displays a concave-down shape that becomes sharper with increasing system size in the vicinity of the percolation threshold, revealing a common underlying scale associated with the transition.

 doi:10.20944/preprints202604.0362.v1

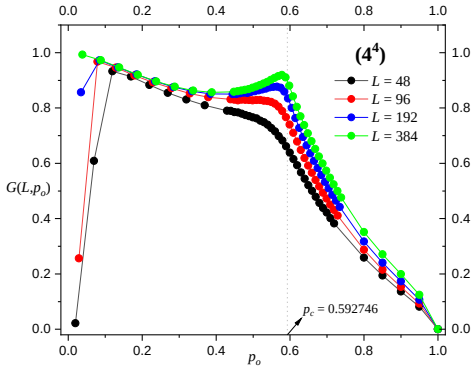

Figure 8. Gini coefficient G as a function of the occupation probability p_0 for different system sizes L. As the system is diluted, G increases, indicating the emergence of transport heterogeneity. The maximum value of G grows with system size, although the curves tend to approach each other for large L, suggesting a saturation behavior. No crossing point is observed near the percolation threshold, indicating that G does not directly capture criticality.

However, a clear distinction emerges when comparing the three observables. While both BC^N_{max} and $p90$ attain their maxima close to the percolation threshold—reflecting the increasing importance of highly central nodes near criticality—the Gini coefficient behaves differently: although its region of strongest curvature remains near p_c, its maximum is systematically shifted towards the subcritical regime.

Taken together, these results show that the signatures of criticality depend on the level at which the betweenness centrality distribution is probed. The observable BC^N_{max} captures the behavior of the most central node and provides a sharp and well-localized indicator of the transition. The percentile p_{90} reflects the collective behavior of the upper tail, yielding a broader and slightly shifted peak. In contrast, the Gini coefficient probes the full distribution and captures the regime of maximal transport heterogeneity, which does not coincide with the critical point.

3.3. Scaling of the Maximum Betweenness at the Critical Occupied Concentration

To characterize the scaling properties of transport localization, we analyze the behavior of the unnormalized maximum betweenness centrality at the vacancy concentration corresponding to the percolation threshold p_c specific to each lattice —that is, the concentration of occupied sites at the critical point. Our goal is to demonstrate that, in the thermodynamic limit ($L \to \infty$), the finite-size pseudo-critical points $p_0^c(L)$, determined by the maximum of BC_{max}, converge to p_c with the same correlation length exponent $\nu = 4/3$ that governs criticality in standard percolation.

Table 3 reports the measured values of $BC_{max}(L, p_c)$ together with their standard errors $ESTD$ for all system sizes and for each Archimedean lattice considered. In all cases, the maximum betweenness increases systematically with system size, reflecting the growing number of shortest paths that traverse the transport backbone at criticality. This scaling behavior indicates that, in absolute terms, transport becomes increasingly concentrated on a small subset of nodes as the system size increases, consistent with the emergence of critical bottlenecks associated with the fractal structure of the incipient infinite cluster.

Table 3. Maximum unnormalized betweenness centrality $BC_{max}(L, p_c) \pm ESTD$ measured at the critical occupied sites concentration p_c for each Archimedean lattice and system size L. The corresponding standard error $ESTD$, obtained from independent realizations of the dilution process, is also reported.

L	BC_{max} square	BC_{max} triangular	BC_{max} kagome	BC_{max} ext. kagome
48	30144 ± 33	21327 ± 24	16933 ± 17	7152 ± 7
96	40744 ± 466	292707 ± 332	232744 ± 248	97973 ± 94
192	5541329 ± 6473	4004270 ± 4651	2558664 ± 2852	1323713 ± 1360
384	$7.556531E7 \pm 90049$	$5.484396E7 \pm 64728$	$4.364242E7 \pm 50600$	$1.802341E7 \pm 19544$

 doi:10.20944/preprints202604.0362.v1

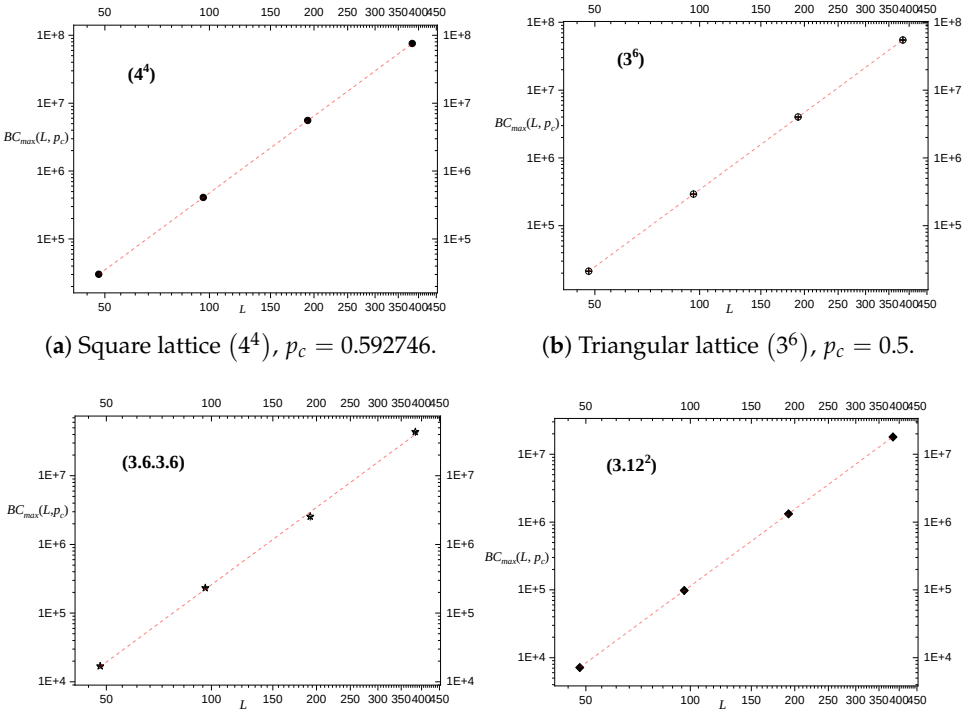

(**a**) Square lattice (4^4), $p_c = 0.592746$. (**b**) Triangular lattice (3^6), $p_c = 0.5$.

(**c**) Kagome lattice $(3.6.3.6)$, $p_c = 0.652703$. (**d**) Extended Kagome lattice (3.12^2), $p_c = 0.8079$.

Figure 9. Log–log representation of the maximum unnormalized betweenness centrality, $BC_{max}(p_c)$, as a function of system size L, evaluated at the occupied concentration p_c corresponding to the thermodynamic percolation threshold of each lattice. Symbols represent numerical results and red dashed lines indicate power-law fits of the form $BC_{max}(p_c) \sim L^{\alpha}$.

This behavior is clearly revealed in the log–log plots shown in Figure 9(a-d), where $BC_{max}(L, p_c)$ is plotted as a function of the system size L for the square (4^4), triangular (3^6), kagome $(3.6.3.6)$, and extended kagome lattices (3.12^2). In each case, the data are well described by a power-law dependence of the form

$$BC_{max}(L, p_c) = AL^{\alpha} \tag{9}$$

where A is a lattice-dependent prefactor and α is a scaling exponent.

Linear fits in log–log scale, shown as red dashed lines in Figure 9(a–d), provide precise estimates of the exponent α, summarized in Table 4. The measured values are

$$\alpha = 3.764 \pm 0.002, 3.7760 \pm 0.0007, 3.74 \pm 0.08, 3.766 \pm 0.003$$

for the square, triangular, kagome, and extended kagome lattices, respectively.

Table 4. Scaling exponent α characterizing the system-size dependence of the maximum unnormalized betweenness centrality at the critical occupied concentration, defined by $BC_{max}(L, p_c) \sim L^{\alpha}$ for each Archimedean lattice. The exponent α is obtained from least-squares fits in log–log scale. Reported uncertainties correspond to the standard error of the fit.

Lattice	$\alpha \pm ESTD$
Square	3.764 ± 0.002
Triangular	3.7760 ± 0.0007
Kagome	3.74 ± 0.08
Ext kagome	3.766 ± 0.003

 doi:10.20944/preprints202604.0362.v1

Despite differences in local connectivity and geometric structure, all lattices exhibit remarkably similar scaling exponents. Within numerical uncertainty, these results indicate a robust algebraic scaling of the form

$$BC_{max}(L, p_c) \sim L^{-\alpha} \tag{10}$$

with

$$\alpha \approx 3.74 - 3.78 \tag{11}$$

This consistent behavior across distinct Archimedean lattices suggests that the scaling of maximum transport load at the pseudo-critical regime is largely insensitive to microscopic lattice details and reflects an intrinsic property of transport organization under site dilution.

Importantly, the observed increase of BC_{max} with increasing system size indicates that transport becomes progressively more concentrated in absolute terms as the system grows. This behavior reflects the growing number of shortest paths that are funneled through a small subset of nodes at criticality. Nevertheless, the persistence of algebraic scaling demonstrates that transport heterogeneity remains governed by scale-dependent structural constraints, even in large systems.

These results provide quantitative evidence that transport localization near the pseudo-critical regime exhibits well-defined finite-size scaling behavior across Archimedean lattices.

3.4. Finite-size Scaling Collapse Of Transport Localization

To further characterize the critical nature of transport localization, we examine the finite-size scaling behavior of the maximum betweenness centrality over the full range of occupation concentrations, following standard scaling arguments in critical phenomena and percolation theory [4,13]. Motivated by scaling theory, we propose that $BC_{max}(L, p_o)$ obeys the scaling form

$$BC_{max}(L, p_o) = L^{\alpha} F\left[(p_o - p_c)L^{1/\nu}\right] \tag{12}$$

where $F(x)$ is a universal scaling function, p_c is the site percolation threshold of the corresponding lattice, ν is the correlation length critical exponent, and α is the exponent determined in Section 3.3.

To test this hypothesis, we plot the rescaled quantity $BC_{max}(L, p_o)/L^{\alpha}$as a function of the scaling variable $(p_o - p_c)L^{1/\nu}$. The results are shown in Figure 10, where panels (a)–(d) correspond to the square, triangular, kagome, and extended kagome lattices, respectively.

Preprints.org (www.preprints.org) | NOT PEER-REVIEWED | Posted: 6 April 2026 doi:10.20944/preprints202604.0362.v1

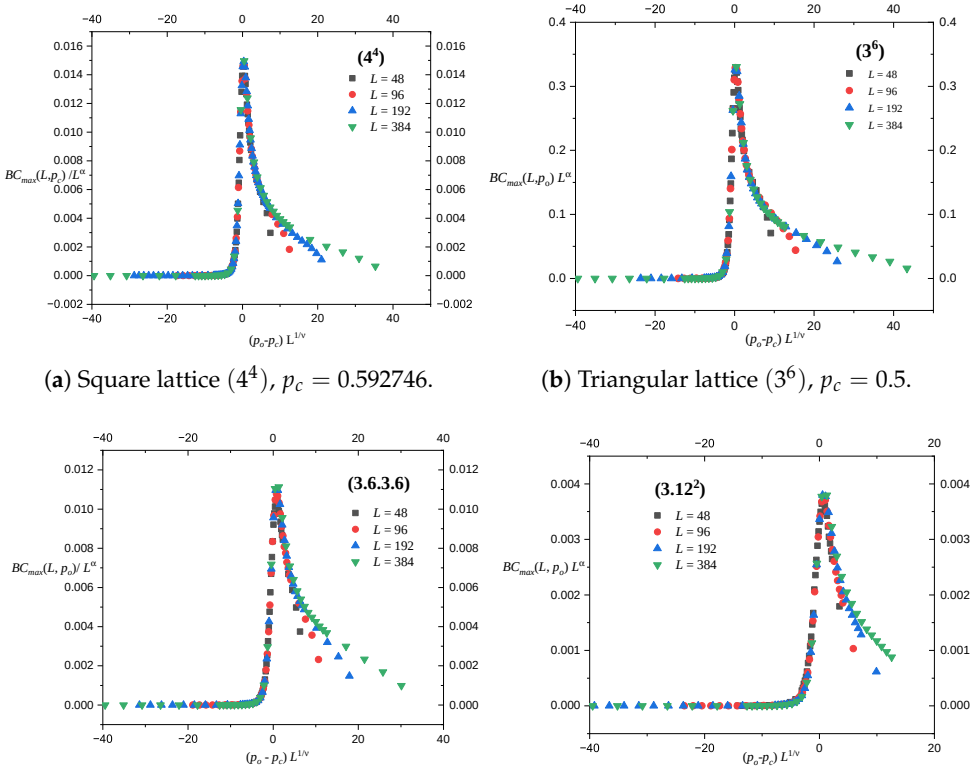

(**a**) Square lattice (4^4), $p_c = 0.592746$. (**b**) Triangular lattice (3^6), $p_c = 0.5$.

(**c**) Kagome lattice $(3.6.3.6)$, $p_c = 0.652704$. (**d**) Extended kagome lattice (3.12^2), $p_c = 0.8079$.

Figure 10. Finite-size scaling collapse of the maximum betweenness centrality for the (a) square, (b) triangular, (c) kagome, and (d) extended kagome lattices. The rescaled quantity $BC_{max}(L, p_o)/L^{\alpha}$ is plotted as a function of the scaling variable $(p_o - p_c)L^{1/\nu}$, where p_c is the percolation threshold of each lattice, ν is the correlation length critical exponent, and α is the exponent determined from the critical scaling analysis. The collapse of curves corresponding to different system sizes onto a single master curve confirms the validity of the proposed scaling form and demonstrates the scale-invariant nature of transport localization near the pseudo-critical regime.

For each lattice, the curves corresponding to different system sizes collapse onto a well-defined master curve over a broad range of the scaling variable. This collapse confirms the validity of the proposed scaling form and demonstrates that transport localization near the pseudo-critical point is governed by scale-invariant mechanisms. In particular, the collapse shows that the growth and subsequent decay of BC_{max} with dilution are controlled by a single characteristic scaling variable, reflecting the emergence of long-range correlations in the transport backbone.

The scaling function exhibits a pronounced maximum near the origin, corresponding to the pseudo-critical regime where transport becomes highly localized and dominated by bottleneck structures. Away from this region, the rescaled betweenness decreases smoothly toward both limits of low and high dilution, consistent with the recovery of more homogeneous transport at low vacancy concentrations and the suppression of global transport near fragmentation.

For the kagome and extended kagome lattices, a slight residual shift of the collapse curves relative to the origin can be observed, with the maxima appearing marginally displaced toward positive values of the scaling variable. This small deviation is within numerical uncertainty and is most likely attributable to finite-size effects and the increased structural complexity of these lattices, which may enhance subleading corrections to scaling. Importantly, this effect remains weak and does not affect the overall quality of the collapse nor the validity of the scaling hypothesis.

The successful collapse observed across all four Archimedean lattices provides strong evidence that the transport pseudo-critical point is governed by universal finite-size scaling behavior. These results confirm that transport localization under random dilution constitutes a genuine critical phe-

 doi:10.20944/preprints202604.0362.v1

nomenon, characterized by scaling laws analogous to those observed in standard percolation, but arising from the collective organization of shortest-path transport structures.

3.5. Transport Backbone Structure and its Relation to the Largest Cluster

3.5.1. Scaling of the Largest Cluster at Criticality

To establish the scaling properties of the transport backbone, we first analyze the behavior of the largest cluster as a function of system size. This quantity characterizes the spatial extent of the connected structure supporting long-range transport and plays a central role in determining the scaling of transport observables.

For each Archimedean lattice, we evaluate the size of the unnormalized maximum cluster, denoted by S_{max}, at the critical occupied concentration p_c, corresponding to the percolation critical point identified in the thermodynamic limit. The measured values of $S_{max}(L, p_c)$ for each lattice and system size are reported in Table 5, together with their corresponding statistical uncertainties.

Table 5. Measured values of the size of the largest connected cluster $S_{max}(L, p_c)$ at the percolation threshold p_c for each Archimedean lattice and system size L. The values correspond to the average over independent realizations, and the reported uncertainties indicate the associated statistical errors. The growth of S_{max} with system size reflects the emergence of the incipient infinite cluster at criticality.

L	$S_{max} \pm ESTD$ square	$S_{max} \pm ESTD$ triangular	$S_{max} \pm ESTD$ kagome	$S_{max} \pm ESTD$ ext. kagome
48	282.605 ± 0.136	242.04 ± 0.11	197.26 ± 0.15	131.41 ± 0.09
96	1041.16 ± 0.54	897.31 ± 0.45	733.04 ± 0.6	485.85 ± 0.36
192	3861.6 ± 2.2	3324.3 ± 1.8	2714.95 ± 2.33	1772.85 ± 1.43
384	14319.1 ± 8.4	12339.2 ± 7.1	10041 ± 8.9	6519 ± 6

Figure 11 shows $S_{max}(L, p_c)$ as a function of system size in log–log scale. In all cases, the data follow a clear power-law dependence of the form

$$S_{max}(L, p_c) = bL^{d_f} \tag{13}$$

where b is a non-universal prefactor and d_f is the fractal dimension of the largest cluster.

 doi:10.20944/preprints202604.0362.v1

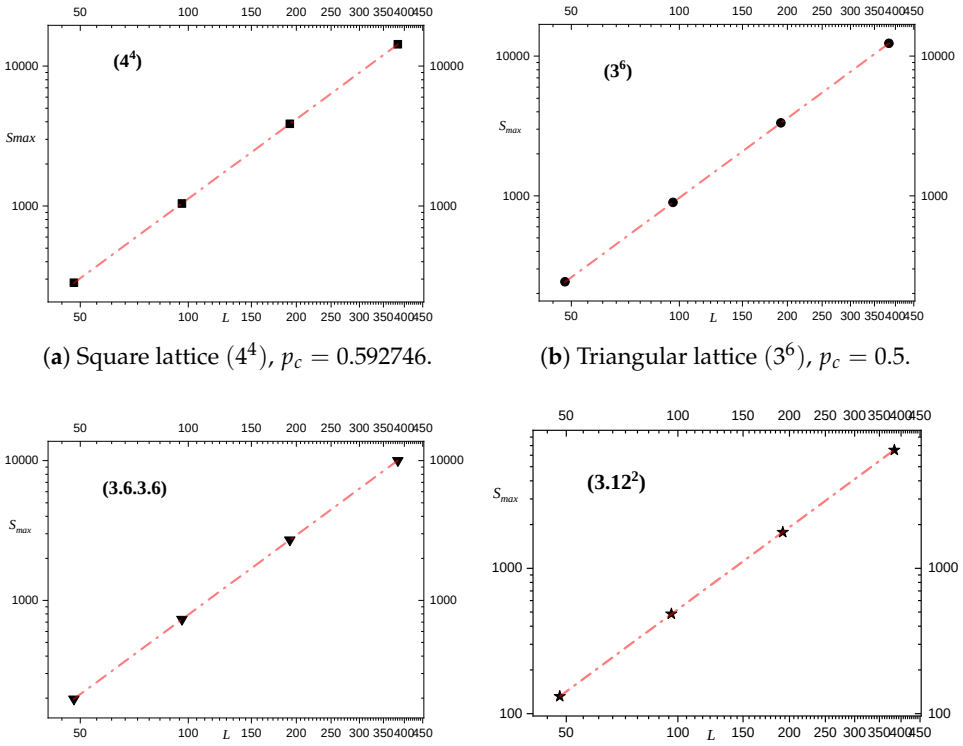

(**a**) Square lattice (4^4), $p_c = 0.592746$.

(**b**) Triangular lattice (3^6), $p_c = 0.5$.

(**c**) Kagome lattice $(3.6.3.6)$, $p_c = 0.652704$.

(**d**) Extended kagome lattice (3.12^2), $p_c = 0.8079$.

Figure 11. Log–log plot of the largest cluster size, $S_{max}(L, p_c)$, as a function of system size L, evaluated at the reference occupied concentration p_c, for the Archimedean lattices considered. In all cases, a clear power-law scaling of the form $S_{max}(L, p_c) \sim L^{d_f}$ is observed, where $d_f$is the fractal dimension of the largest cluster. The red dashed lines represent least-squares fits to the power-law scaling.

The exponent d_f is obtained from linear fits in log–log scale, and the resulting values for each lattice are summarized in Table 6.

Table 6. Scaling exponent d_f characterizing the system-size dependence of the unnormalized maximum cluster at the critical occupied concentration p_c, defined by $S_{max}(L, p_c) \sim L^{-d_f}$ for each Archimedean lattice. The exponent d_f is obtained from least-squares fits in log–log scale. Reported uncertainties correspond to the standard error of the fit.

Lattice	$d_f \pm ESTD$
Square	1.888 ± 0.002
Triangular	1.89045 ± 0.00036
Kagome	1.8899 ± 0.0011
Extended kagome	1.877 ± 0.003

The resulting values are

$$d_f = 1.888 \pm 0.002, 1.89045 \pm 0.00036, 1.8899 \pm 0.0011, 1.877 \pm 0.003,$$

for the four Archimedean lattices considered.

The data exhibit excellent agreement with the power-law scaling over the full range of system sizes investigated, and are in very good agreement with the theoretical fractal dimension of the critical percolation cluster in two dimensions [4],

$$d_f = \frac{91}{48} \approx 1.895833 \tag{14}$$

 doi:10.20944/preprints202604.0362.v1

confirming that the pseudo-critical regime identified through transport observables corresponds to the percolation critical regime. Minor deviations observed for some lattices can be attributed to finite-size effects and residual corrections to scaling.

The consistency between the measured and theoretical values of d_f provides strong evidence that the transport backbone at pseudo-criticality is a scale-invariant fractal object. As shown in the following subsection, this fractal structure directly governs the scaling relationship between maximum betweenness centrality and the size of the largest cluster.

3.5.2. Scaling Relation Between Maximum Betweenness Centrality and Largest Cluster Size

We now examine the relationship between the maximum betweenness centrality and the size of the largest cluster at the critical occupation fraction p_c. At criticality, the size of the largest cluster with system size as $S_{max} \sim L^{d_f}$, reflecting the fractal nature of the incipient infinite cluster [4]. In this analysis, we consider the unnormalized maximum betweenness centrality, denoted as BC_{max}, in order to avoid the influence of normalization factors that depend explicitly on system size.

Figure 12 shows log–log plots of BC_{max} as a function of the largest cluster size S_{max} for the four Archimedean lattices considered. Each panel corresponds to a different lattice geometry, and the numerical values used to construct these plots are reported in Table 7, which contains four subtables (a)–(d), one for each lattice.

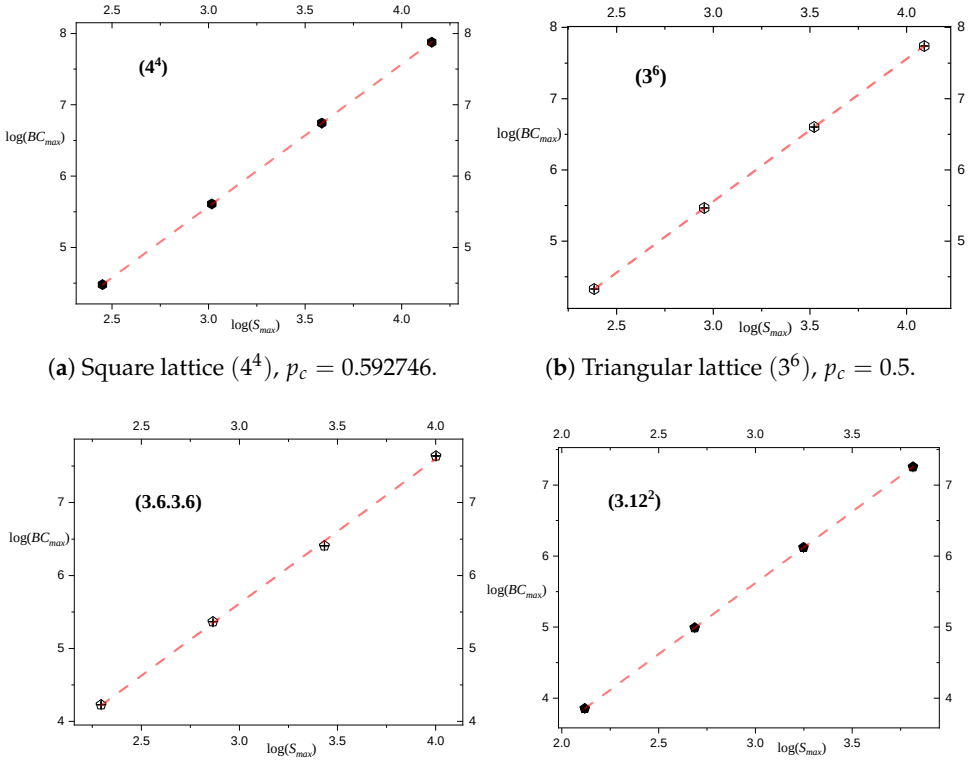

(**a**) Square lattice (4^4), $p_c = 0.592746$. (**b**) Triangular lattice (3^6), $p_c = 0.5$.

(**c**) Kagome lattice $(3.6.3.6)$, $p_c = 0.652704$. (**d**) Extended kagome lattice (3.12^2), $p_c = 0.8079$.

Figure 12. Log–log plots of the unnormalized maximum betweenness centrality, BC_{max}, as a function of the size of the unnormalized largest cluster, S_{max}, both quantities evaluated at p_c, for the four Archimedean lattices considered. (a) Square lattice (4^4), $p_c = 0.592746$, (b) Triangular lattice (3^6), $p_c = 0.5$, Kagome lattice $(3.6.3.6)$, $p_c = 0.652704$, (d) Extended kagome lattice (3.12^2), $p_c = 0.8079$. The approximately linear behavior observed in all cases indicates power-law scaling of the form $BC_{max} \sim (S_{max})^{\beta}$. The red dashed lines correspond to least-squares linear fits in log–log scale. The fitted exponents are reported in Table 8.

 doi:10.20944/preprints202604.0362.v1

Table 7. Measured values of the unnormalized largest cluster size S_{max} and the unnormalized maximum betweenness centrality BC_{max} at the critical occupation probability p_c for different system sizes L. Subtables (a)–(d) correspond to the square, kagome, extended kagome, and triangular lattices, respectively. For each system size, the table reports the mean value, and the standard error of the mean ($ESTD$), computed over 100000 independent realizations.

a Square lattice, $p_c = 0.592746$

Square: (4^4)		
L	$S_{max} \pm ESTD$	$BC_{max} \pm ESTD$
48	282.60 ± 0.14	30144 ± 33
96	1041.16 ± 0.54	407442 ± 466
192	3861.60 ± 2.15	5541329 ± 6473
384	14319.10 ± 81.37	75565310 ± 90049

b Triangular lattice, $p_c = 0.5$

Triangular: (3^6)		
L	$S_{max} \pm ESTD$	$BC_{max} \pm ESTD$
48	242.04 ± 0.11	21327 ± 24
96	897.31 ± 0.45	2927067 ± 332
192	3324.30 ± 1.82	4004270 ± 4651
384	12339.20 ± 7.11	54843960 ± 64728

c Kagome lattice, $p_c = 0.652703$

Kagome: $(3.6.3.6)$		
L	$S_{max} \pm ESTD$	$BC_{max} \pm ESTD$
48	197.26 ± 0.15	16933 ± 17
96	733.04 ± 0.60	232744 ± 248
192	2714.95 ± 2.33	2558664 ± 2852
384	10041.00 ± 8.89	43642420 ± 50601

d Extended kagome lattice, $p_c = 0.8079$

Extended kagome: (3.12^2)		
L	$S_{max} \pm ESTD$	$BC_{max} \pm ESTD$
48	$131,41 \pm 0.09$	7152 ± 6
96	$485,85 \pm 0.37$	97973 ± 94
192	$1772,85 \pm 1.44$	1323713 ± 1360
384	$6519,00 \pm 5.53$	18023410 ± 19544

In all cases, a clear linear behavior is observed in log–log scale over the full range of accessible system sizes, indicating a power-law relationship between these quantities. This scaling relation can be expressed as

$$BC_{max} \sim (S_{max})^{\beta} \tag{15}$$

where β is the corresponding scaling exponent.

The values of the exponent β are obtained from linear fits to the data in log–log representation and are summarized in Table 8 for each lattice.

Table 8. Scaling exponents β obtained from least-squares fits of the power-law relation between the unnormalized maximum betweenness centrality and the size of the largest cluster, $BC_{max} \sim (S_{max})^{\beta}$. The exponents were extracted from the slopes of the linear fits in the log–log plots shown in Figure 12 for each Archimedean lattice considered. The reported uncertainties correspond to the standard error of the fit.

Lattice	$\beta \pm ESTD$
Square	1.994 ± 0.002
Triangular	1.997 ± 0.001
Kagome	1.98 ± 0.04
Ext kagome	2.006 ± 0.002

The measured exponents are

$$\beta = 1.994 \pm 0.002, 1.997 \pm 0.001, 1.98 \pm 0.04, \text{and } 2.006 \pm 0.002$$

for the square, kagome, extended kagome, and triangular lattices, respectively. Within numerical uncertainty, all values are consistent with the exact scaling relation $\beta = 2$, indicating that the maximum betweenness centrality grows quadratically with the size of the largest cluster, independently of lattice geometry.

This result shows that the growth of the maximum betweenness centrality is directly governed by the growth of the largest cluster, revealing a fundamental connection between transport heterogeneity and connectivity at criticality. Importantly, this scaling relation is consistently observed across all Archimedean lattices considered, demonstrating its robustness with respect to lattice geometry.

 doi:10.20944/preprints202604.0362.v1

The quadratic scaling of the maximum betweenness centrality with the size of the largest cluster establishes a direct and robust connection between transport bottlenecks and the underlying percolation structure. This result indicates that the most constraining transport nodes emerge from correlations that extend across the spanning backbone, and that their strength increases superlinearly with the characteristic size of the connected structure.

While the scaling relations presented above characterize the average behavior of the system, a complete description of the critical regime also requires examining the fluctuations of the maximum betweenness centrality. In particular, the variance of BC_{max} provides information about the stability of transport pathways and the emergence of large-scale variability near criticality. In the following section, we present a quantitative analysis of the finite-size scaling of the transport susceptibility associated with maximum betweenness centrality introduced in Section 3.1.3.

3.6. Susceptibility of Maximum Betweenness Centrality

3.6.1. Scaling of the Susceptibility of The Maximum Betweenness Centrality

In this subsection we analyze the scaling behavior of the fluctuations of the transport bottleneck at criticality. In analogy with standard definitions in critical phenomena [4], we define the transport susceptibility, as anticipated in Section 3.1.3, as the variance of the unnormalized maximum betweenness centrality,

$$\chi(L, p_c) = \mathrm{var}(BC_{max}(L, p_c)) \tag{16}$$

evaluated at the reference occupation probability p_c for each lattice, where BC_{max} is the unnormalized maximum betweenness centrality.

Figure 13 shows the log–log plots of $\chi(L)$ as a function of the system size L for the four Archimedean lattices considered.

In all cases, a clear linear behavior is observed over the full range of system sizes, indicating power-law scaling of the form

$$\chi(L) \sim L^{\gamma} \tag{17}$$

Table 9 reports the measured values of $\chi(L, p_c)$ for all system sizes and for each Archimedean lattice considered.

Table 9. transport susceptibility $\chi(L, p_c)$ measured at the critical vacancy concentration p_c for each Archimedean lattice and system size L.

L	χ square	χ triangular	χ kagome	χ Ext. kagome
48	1,087469E+8	5,533892E+7	2,899058E+7	4,168138E+6
96	2,171602E+10	1,104305E+10	6,144178E+9	8,836108E+8
192	4,189956E+12	2,16292E+12	8,135926E+11	1,849461E+11
384	8,108865E+14	4,189777E+14	2,560442E+14	3,819853E+13

Linear fits in log–log scale, shown as red lines in Figure 13(a–d), provide precise estimates of the exponent γ, summarized in Table 10.

Table 10. Scaling exponent γ characterizing the system-size dependence of the transport susceptibility at the critical occupied concentration p_c, defined by $\chi(L, p_c) \sim L^{-\gamma}$ for each Archimedean lattice. The exponent γ is obtained from least-squares fits in log–log scale. Reported uncertainties correspond to the standard error of the fit.

Lattice	$\gamma \pm ESTD$
Square	7.608 ± 0.008
Triangular	7.617 ± 0.007
Kagome	7.6 ± 0.2
Ext kagome	7.709 ± 0.006

 doi:10.20944/preprints202604.0362.v1

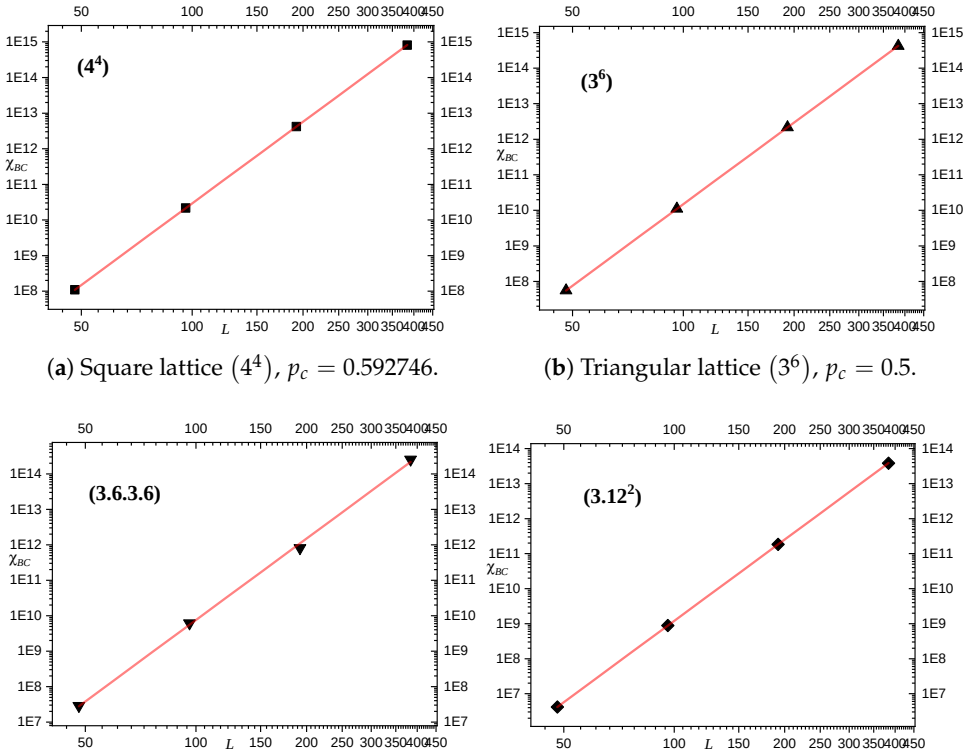

(**a**) Square lattice (4^4), $p_c = 0.592746$.

(**b**) Triangular lattice (3^6), $p_c = 0.5$.

(**c**) Kagome lattice $(3.6.3.6)$, $p_c = 0.652703$.

(**d**) Extended Kagome lattice (3.12^2), $p_c = 0.8079$.

Figure 13. Log–log representation of the transport susceptibility, $\chi(L, p_c)$, as a function of system size L, evaluated at the occupied concentration p_c corresponding to the thermodynamic percolation threshold of each lattice. Symbols represent numerical results and red dashed lines indicate power-law fits of the form $\chi(L, p_c) \sim L^{\gamma}$. (a) Square lattice (4^4), $p_c = 0.592746$, (b) Triangular lattice (3^6), $p_c = 0.5$, (c) Kagome lattice $(3.6.3.6)$, $p_c = 0.652703$, (d) Extended Kagome lattice (3.12^2), $p_c = 0.8079$.

 doi:10.20944/preprints202604.0362.v1

The measured values are

$$\gamma = 7.608 \pm 0.008, 7.617 \pm 0.007, 7.6 \pm 0.2, 7.709 \pm 0.006$$

for the square, triangular, kagome, and extended kagome lattices, respectively.

Within numerical uncertainty, these values are statistically indistinguishable, providing strong evidence that the scaling of the transport fluctuations is universal across the different lattice geometries.

This behavior is fully consistent with the hierarchical scaling relations established in previous sections. We have shown that the largest cluster scales as

$$Smax \sim L^{d_f},$$

with $d_f \approx 1.89$, and that the unnormalized maximum betweenness centrality obeys

$$BC_{max} \sim S_{max}^2.$$

Combining these relations yields

$$BC_{max} \sim L^{2d_f}.$$

Under the standard scaling assumption that fluctuations scale with the square of the characteristic magnitude, one expects

$$\chi(L) = var(BC_{max}) \sim L^{4d_f}.$$

Using the measured value $d_f \approx 1.89$, this prediction gives

$$4d_f \approx 7.56,$$

in excellent agreement with the numerically measured exponent γ.

Therefore, the scaling of the transport susceptibility is governed by the same fractal geometry that controls the growth of the maximum cluster and the transport bottleneck itself. The results indicate that the fluctuations of the maximum betweenness centrality are critical and strongly amplified with increasing system size, following a universal power-law behavior independent of lattice topology.

3.6.2. Finite-size Scaling Collapse of The Transport Susceptibility

In Section 3.6.1 we established that, at the reference occupation probability p_c, the transport susceptibility scales as $\chi(L) \sim L^{\gamma}$. We now examine whether this behavior is compatible with a full finite-size scaling description in the vicinity of p_c, as expected for critical systems in percolation theory [4,13].

Assuming standard finite-size scaling near criticality, we consider the ansatz

$$\chi(L, p_o) = L^{\gamma} F\left((p_o - p_c)L^{1/\nu}\right), \tag{18}$$

where F is a universal scaling function and ν is the correlation length exponent. For two-dimensional percolation, $\nu = 4/3$.

Accordingly, we rescale the data as

$$\frac{\chi(L,po)}{L^{\gamma}} \text{ versus } (p_o - p_c)L^{1/\nu},$$

using the percolation thresholds p_c for each lattice, together with $\gamma \approx 7.6$ and $\nu = 4/3$.

The resulting collapses are shown in Figure 14, panels (a)–(d), corresponding to the square, kagome, extended kagome, and triangular lattices, respectively.

In all cases, data obtained for different system sizes collapse onto a single master curve within numerical accuracy, providing strong support for the proposed finite-size scaling form.

 doi:10.20944/preprints202604.0362.v1

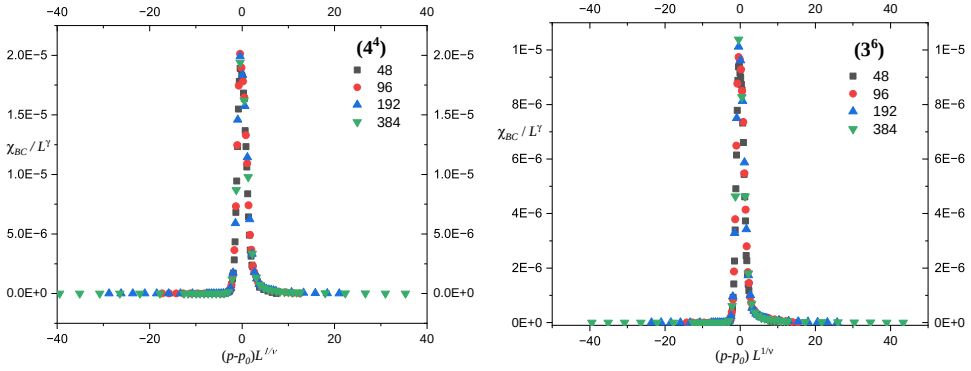

(**a**) Square lattice (4^4), $p_c = 0.592746$. (**b**) Triangular lattice (3^6), $p_c = 0.5$.

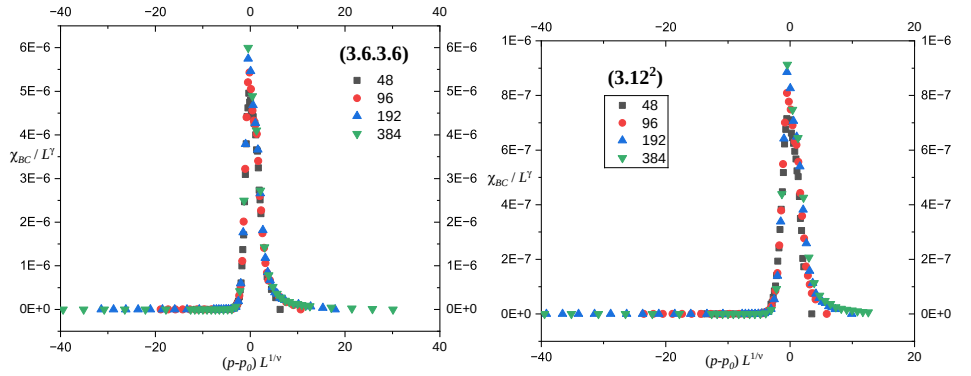

(**c**) Kagome lattice $(3.6.3.6)$, $p_c = 0.652703$. (**d**) Extended Kagome lattice (3.12^2), $p_c = 0.8079$.

Figure 14. Finite-size scaling collapse of the transport susceptibility $\chi(L, p_c)$ for different system sizes L. (a) Square lattice, (b) triangular lattice, (c) kagome lattice, and (d) extended kagome lattice. The rescaling $\chi(L, p_c) \sim L^{\gamma}$ leads to a satisfactory collapse of the data onto a single universal curve for each lattice. This behavior demonstrates that the fluctuations of the transport bottleneck are governed by the same critical scaling framework as geometric percolation.

 doi:10.20944/preprints202604.0362.v1

This collapse indicates that the fluctuations of the unnormalized maximum betweenness centrality are governed by the same critical exponents that control the underlying geometric percolation transition.

Taken together, the consistency between the critical scaling $\chi(L) \sim L^{\gamma}$ established in Section 3.6.1 and the full finite-size scaling form demonstrates that the transport susceptibility follows the universal scaling structure of two-dimensional percolation. This result reinforces the interpretation of transport fluctuations as a genuine critical observable, fully determined by the fractal geometry and long-range correlations of the system at criticality.

This demonstrates that transport criticality is not confined to extreme events, but is encoded in the full fluctuation structure of the system.

3.7. Finite-size Behavior of The Transport Pseudo-critical Point

The location $p_o^c(L)$ of the maximum of $BC_{max}^N(L, p_o)$ depends systematically on the system size, as expected for pseudo-critical points in finite systems [4]. In this framework, the shift of the pseudo-critical point is expected to follow

$$p_o^c(L) = p_c + aL^{-1/\nu} \tag{19}$$

where p_c is the critical occupation probability in the thermodynamic limit and ν is the correlation-length exponent.

Figure 15 shows the evolution of $p_o^c(L)$ for the square lattice as a function of the linear size L. Panel (a) displays $p_o^c(L)$ as a function of the linear size L for $120 \leq L \leq 384$, together with a nonlinear fit used to estimate the asymptotic value of the threshold. Panel (b) shows the same data replotted against $L^{-1/\nu}$, revealing the expected linear behavior.

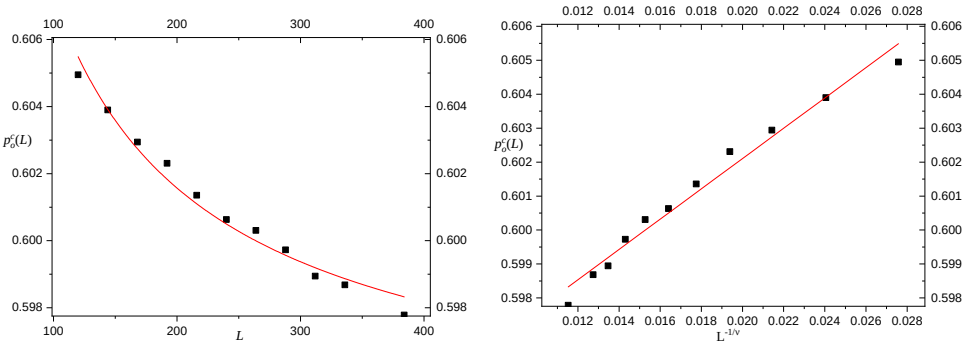

(**a**) Finite-size behavior of $p_o^c(L)$ as a function of the system size L for $120 \leq L \leq 384$.

(**b**) Same data replotted as a function of $L^{-1/\nu}$, with $\upsilon = 4/3$.

Figure 15. Finite-size behavior of the pseudo-critical occupation probability $p_o^c(L)$ for the square lattice. (a) $p_o^c(L)$ as a function of the linear size L for $120 \leq L \leq 384$. The solid line corresponds to a nonlinear fit used to estimate the asymptotic critical point in the thermodynamic limit. (b) The same data as in panel (a), replotted as a function of $L^{-1/\nu}$, with $\upsilon = 4/3$, illustrating the expected finite-size scaling behavior.

A linear extrapolation in $L^{-1/\nu}$ yields an estimate $p_c = 0.59319 \pm 0.0004$, with a coefficient of determination $R^2 = 0.97778$. While this result suggests convergence toward a value close to the geometric critical occupation fraction of the square lattice, the present analysis should be interpreted with caution.

The values $p_o^c(L)$ were obtained by averaging over 10^4 independent realizations. However, the maximum of BC_{max} is associated with large sample-to-sample fluctuations, which lead to a relatively broad dispersion of the peak position. As a consequence, the estimated pseudo-critical points $p_o^c(L)$ may still contain significant statistical uncertainty.

 doi:10.20944/preprints202604.0362.v1

For this reason, the trends observed in Figure 15 should be regarded as indicative rather than conclusive. While the detailed finite-size scaling analysis is presented here for the square lattice, qualitatively similar behavior is observed across all the Archimedean lattices considered. For the sake of clarity and to avoid redundancy, we restrict the quantitative analysis to this representative case. A more accurate determination of the finite-size scaling behavior will likely require increasing both the number of realizations and the range of system sizes explored in future simulations.

4. Discussion

The results presented in this work reveal that transport organization in disordered spatial networks exhibits well-defined critical features that closely mirror those of classical percolation [4,13]. While percolation theory traditionally focuses on the emergence of large-scale connectivity, our analysis shows that the redistribution of shortest-path transport provides an alternative and complementary perspective on the transition. In particular, the existence of a transport pseudo-critical point, identified through the maximization of betweenness centrality, indicates that the system undergoes a sharp reorganization of flow patterns prior to the complete loss of global connectivity.

Betweenness centrality has long been used as a proxy for load, congestion, and vulnerability in complex networks [1,2], particularly in the context of communication and transportation systems. Previous studies have highlighted its relevance for identifying critical nodes and assessing network robustness. However, its behavior under controlled structural disorder, and especially its relation to critical phenomena such as percolation, has received comparatively less attention. The present results demonstrate that the maximal betweenness and its fluctuations obey finite-size scaling forms consistent with the universal exponents of two-dimensional percolation [4,13]. This establishes a direct connection between geometric criticality and transport organization, showing that the onset of large-scale connectivity is accompanied by a pronounced localization of shortest-path flows.

Importantly, this transport localization is not limited to a single extremal node. Complementary observables, such as the percentile (p_{90}) and the Gini coefficient, indicate that the reorganization of transport involves a broader subset of nodes and manifests across multiple scales. Near the critical regime, a finite fraction of highly central nodes contributes significantly to the transport backbone, while global measures of inequality reveal a marked increase in load heterogeneity. These observations suggest that transport criticality is inherently a collective phenomenon, reflecting the interplay between network topology and the distribution of shortest-path routes.

From a broader perspective, these findings highlight that connectivity-based descriptions alone are insufficient to fully characterize functional behavior in spatial networks. Two systems with similar levels of connectivity may exhibit markedly different transport organizations, depending on how shortest paths are distributed. In this sense, transport observables provide additional insight into the internal structure of connected components, particularly in regimes where the system is close to fragmentation.

Finally, some limitations of the present study should be noted. The determination of pseudo-critical points and scaling exponents is affected by finite-size effects and statistical fluctuations, especially near the transition. While the qualitative behavior is robust across all Archimedean lattices considered, a more precise quantitative characterization would benefit from larger system sizes and improved sampling. Future work could also explore the role of weighted or directed transport, as well as the extension of these ideas to more heterogeneous or real-world network topologies.

Overall, the framework developed here provides a unified perspective for understanding how transport reorganizes under structural disorder, bridging the gap between geometric percolation and functional flow processes in complex networks.

5. Conclusions

In this work we investigated how transport reorganizes in site-diluted Archimedean lattices by analyzing the behavior of the maximum betweenness centrality under progressive disorder. Rather than

 doi:10.20944/preprints202604.0362.v1

focusing exclusively on geometric connectivity, our approach examines how shortest-path transport becomes redistributed as the network approaches fragmentation.

For all lattices considered, the maximum betweenness centrality exhibits a robust non-monotonic dependence on the occupation probability. Starting from a fully occupied system, the introduction of disorder initially increases the concentration of shortest-path traffic on a small subset of nodes, leading to the emergence of pronounced transport bottlenecks. Beyond a certain dilution level, however, the progressive loss of connectivity suppresses long-range transport and the betweenness decreases. As a result, a well-defined maximum appears at an intermediate occupation probability ($p_o^c(L)$), which defines a transport pseudo-critical point.

A finite-size scaling analysis shows that this pseudo-critical point is governed by the same critical behavior that characterizes classical percolation. In particular, the position of the maximum exhibits a systematic size-dependent drift compatible with the scaling form ($p_o^c(L) = p_c + aL^{-1/\nu}$), with the correlation-length exponent fixed to its two-dimensional value ($\nu = 4/3$). Extrapolations obtained from this scaling are consistent with the known percolation threshold of the square lattice, indicating that the transport pseudo-transition detected through betweenness centrality converges to the standard geometric critical point in the thermodynamic limit.

Beyond the behavior of the pseudo-critical point itself, the transport observables display clear scaling properties near criticality. When expressed in terms of the scaling variable ($(p_o - p_c)L^{1/\nu}$), the curves corresponding to different system sizes collapse onto a common scaling function. This data collapse provides strong evidence that the reorganization of shortest-path transport near the transition is governed by the universal critical scaling of percolation. In this sense, betweenness centrality reveals how the geometric criticality of connectivity is accompanied by a pronounced localization of transport flows.

The fluctuations of the maximum betweenness further support this interpretation. The variance of (BC_{max}), interpreted here as an effective transport susceptibility, exhibits a pronounced peak in the vicinity of the pseudo-critical regime. This behavior reflects the strong realization-to-realization variability of shortest-path structures when the system is poised between global connectivity and fragmentation. In this regime, small structural perturbations can induce large reorganizations of the transport backbone, producing strong fluctuations in the localization of load across the network.

Consistent with this picture, complementary measures of the betweenness distribution further support the interpretation of a transport-driven pseudo-critical regime. The percentile p_{90} exhibits a peak-like behavior in the vicinity of the transition, indicating that not only the most central node but a finite fraction of highly central nodes contributes to the transport backbone. At the same time, global inequality measures such as the Gini coefficient reveal a marked increase in transport heterogeneity near criticality, confirming that the redistribution of shortest-path flows involves a broad range of nodes across the network. Together, these observables provide a multiscale characterization of transport localization, from extreme bottlenecks to collective and system-wide heterogeneity, demonstrating that transport criticality is not confined to extreme nodes, but is a collective phenomenon spanning the full distribution of load.

From the perspective of network resilience, the emergence of strong transport localization near the critical regime has important implications. As the system approaches the percolation threshold, shortest-path transport becomes increasingly concentrated on a small subset of nodes that act as critical bottlenecks. In this regime, the functionality of the network becomes highly sensitive to the failure or removal of a few key nodes, even when a large fraction of the structure remains intact. The peak observed in the transport susceptibility reflects precisely this heightened structural vulnerability, indicating the point where the redistribution of flows becomes maximally unstable under microscopic perturbations.

These observations suggest that transport-based indicators such as betweenness centrality may provide useful tools for identifying fragile operational regimes in spatial networks. In infrastructures where flows follow shortest or near-shortest routes—such as communication systems, transportation

 doi:10.20944/preprints202604.0362.v1

grids, or logistical networks—the concentration of load on a small number of nodes can signal the onset of critical vulnerability. Within this context, the framework developed here offers a complementary perspective for assessing robustness and resilience, linking classical connectivity transitions with the organization of transport backbones that sustain functional flows in complex networks.

More broadly, our results show that the percolation transition can be viewed not only as the emergence of large-scale connectivity, but also as a critical reorganization of transport pathways in spatial networks. In this regime, shortest-path flows become concentrated on a sparse transport backbone, revealing how geometric criticality translates into transport localization.

Author Contributions: All authors contributed equally to this work. All authors have read and agreed to the published version of the manuscript.

Conflicts of Interest: The authors declare no conflicts of interest.

Data Availability Statement: The C++ source code implementing the algorithms described in Section 2 is publicly available at \url{https://github.com/urobal/mdpi_1.git} and archived at Zenodo with DOI \url{https://doi.org/10.5281/zenodo.19305459}. The repository includes the three simulation programs described in Section 2.8, along with documentation and example input files. The code is provided for the purpose of reproducing the results presented in this work. All data generated from the simulations are presented in the figures and tables of this article. No additional external datasets were used or generated.

Acknowledgments: The authors acknowledge the computational resources provided by the Centro de Excelencia de Modelación y Computación Científica (CEMCC) at Universidad de La Frontera, Temuco, Chile, specifically the Lautaro node (40 cores, 64 GB RAM) used in this work. Additional computing facilities were provided by the Instituto de Física Aplicada (INFAP), Universidad Nacional de San Luis, Argentina. The authors thank the staff of both institutions for their technical support.

References

1. Freeman, L.C. A set of measures of centrality based on betweenness. *Sociometry* **1977**, *40*, 35–41.
2. Newman, M.E.J. *Networks: An Introduction*; Oxford University Press: Oxford, 2010.
3. Albert, R.; Jeong, H.; Barabási, A.L. Error and attack tolerance of complex networks. *Nature* **2000**, *406*, 378–382.
4. Stauffer, D.; Aharony, A. *Introduction to Percolation Theory*; Taylor & Francis: London, 1994.
5. Saberi, A.A. Recent advances in percolation theory and its applications. *Physics Reports* **2015**, *578*, 1–32.
6. Newman, M.E.J. *Networks*; Oxford University Press: Oxford, 2018.
7. Barthélemy, M. Spatial networks. *Physics Reports* **2011**, *499*, 1–101.
8. Grünbaum, B.; Shephard, G.C. *Tilings and Patterns*; Courier Dover Publications: New York, 1987.
9. Torres, A.A.; Ramirez-Pastor, J.A. Representation of Archimedean Networks and Inclusion: Computational Applications to Percolation and Network Transitions. *arXiv preprint* **2025**, *arXiv:2507.12229*. arXiv:2507.12229.
10. Parviainen, R.; Wierman, J.C. Inclusions and non-inclusions of Archimedean and Laves lattices. *Electron. J. Comb.* **2003**, *10*, R00.
11. Brandes, U. A faster algorithm for betweenness centrality. *J. Math. Sociol.* **2001**, *25*, 163–177.
12. Kiefer, J. Sequential minimax search for a maximum. *Proc. Amer. Math. Soc.* **1953**, *4*, 502–506.
13. Christensen, K.; Moloney, N.R. *Complexity and Criticality*; Vol. 1, Imperial College Press: London, 2005.